J. Fluid Mech. (1999), *vol.* 387, *pp.* 353–396. Printed in the United Kingdom

Mechanisms for generating coherent packets of hairpin vortices in channel flow

By J. ZHOU, R. J. ADRIAN, S. BALACHANDAR AND T. M. KENDALL†

Department of Theoretical and Applied Mechanics, University of Illinois, Urbana, Illinois 61801, USA

(Received 10 June 1997 and in revised form 22 May 1998)

The evolution of a single hairpin vortex-like structure in the mean turbulent field of a low-Reynolds-number channel flow is studied by direct numerical simulation. The structure of the initial three-dimensional vortex is extracted from the two-point spatial correlation of the velocity field by linear stochastic estimation given a second-quadrant ejection event vector. Initial vortices having vorticity that is weak relative to the mean vorticity evolve gradually into omega-shaped vortices that persist for long times and decay slowly. As reported in Zhou, Adrian & Balachandar (1996), initial vortices that exceed a threshold strength relative to the mean flow generate new hairpin vortices upstream of the primary vortex. The detailed mechanisms for this upstream process are determined, and they are generally similar to the mechanisms proposed by Smith *et al.* (1991), with some notable differences in the details. It has also been found that new hairpins generate downstream of the primary hairpin, thereby forming, together with the upstream hairpins, a coherent packet of hairpins that propagate coherently. This is consistent with the experimental observations of Meinhart & Adrian (1995). The possibility of autogeneration above a critical threshold implies that hairpin vortices in fully turbulent fields may occur singly, but they more often occur in packets. The hairpins also generate quasi-streamwise vortices to the side of the primary hairpin legs. This mechanism bears many similarities to the mechanisms found by Brooke & Hanratty (1993) and Bernard, Thomas & Handler (1993). It provides a means by which new quasi-streamwise vortices, and, subsequently, new hairpin vortices can populate the near-wall layer.

1. Introduction

A central flow feature that can serve as the starting point in the development of a unified picture of the turbulent wall layer is the hairpin or horseshoe vortex. Since the original proposal by Theodorsen (1952), the importance of hairpin or horseshoe-type vortices in turbulent wall layers has become widely, albeit not totally, accepted. In early models, horseshoe vortices were considered to have Ω-shaped head and neck regions that connect the head to long spanwise vortex legs. Subsequent investigations have indicated the vortex structure to be more like a hairpin with a pair of counter-rotating quasi-streamwise vortices near the wall instead of a spanwise vortex (Robinson 1991). The hairpins are not usually observed to posses perfect spanwise symmetry with the two counter-rotating vortex legs of equal strength. Instead, spanwise asymmetric

† Present address: Ballistic Research Laboratory, US Army, Aberdeen Proving Grounds, MD, USA.

one-sided hairpins, also known as 'canes', are often observed (Guezennec & Choi 1989). Nevertheless, a picture of the turbulent wall layer as a distribution of hairpin vortices provides a reasonable explanation for many observed flow features. The long quasi-streamwise legs of the hairpin structures particularly explain the near-wall low-speed streaks. Passage of a rapidly lifting hairpin head and the strong pumping of fluid between the hairpin legs create a burst event with an associated second quadrant velocity fluctuations (Q2 event). Near-wall shear layers can be explained as the result of the low-speed near-wall fluid pumped up between the vortex legs encountering the high-speed free-stream fluid. Perhaps most importantly, the spanwise spacing of low-speed streaks is associated with the spanwise width of the hairpin legs, and the characteristic 30° to 50° angle seen in the structure of wall turbulence is associated with the angle at which hairpins incline with respect to the wall.

Our understanding of the turbulent wall layer based on hairpin-like vortex structures can hardly be considered complete. Important questions still remain unanswered as to how these vortical structures grow from within the buffer layer into the outer regions of the boundary layer. Head & Bandyopadhyay (1981) suggest that narrow, buffer-layer scale hairpin vortices of spanwise width 100 viscous wall units, grow in length and extend from near the wall all the way up to the outer edges of the boundary layer, maintaining approximately the same spanwise size. This picture of hairpin growth implies vortex structures whose height-to-width aspect ratio becomes infinite with Reynolds number. It seems unlikely that such thin vortices can survive in an environment of strong local turbulent eddies. Hence, it is necessary to establish how near-wall vortical structures grow in size and are related to outer-layer vortical structures. Different scenarios are possible: the growth may occur by continuous increase of the lengthscale of the vortex or by discrete steps due to pairing and merger of the vortices or some combination of the two. While the continuous growth model seems simple, as the hairpin vortices grow bigger, the neighbouring vortices must become very close to each other in the spanwise direction and mutual interaction may at some point occur. On the other hand, fundamental questions also exist as to whether the vortex mergers that might occur can produce self-similar vortices or merge to generate a new class of structures. Although a self-similar merger process is appealing, it is difficult to establish conclusively based on our current understanding of the detailed mechanisms. Furthermore, continuous and discrete growth may occur together in the form of hairpin structures growing between successive mergers.

Putting aside questions about vortices extending across the entire layer, our understanding of the organization of hairpin vortices is also far from complete. For example, a number of prominent models of coherent structures in wall turbulence (Bakewell & Lumley 1967; Perry & Chong 1982; Perry, Henbest & Chong 1986) assume that the hairpins are scattered randomly in streamwise and spanwise directions. However, hairpin vortices could occur in groups with a definite spatial arrangement within the group. Support for this view can be seen in the measurements of Bogard & Tiederman (1986), Luchik & Tiederman (1987) and Tardu (1995), where the near-wall burst process was observed to be typically made up of multiple Q2 events. The average length of a low-speed streak associated with a hairpin vortex is about two to three hundred wall units in low-Reynolds-number channel flow (Kim 1983). This is far too short to explain the long streaks that are experimentally observed. Both observations suggest that hairpins sometimes occur in organized groups (or packets) and not always as randomly scattered individuals. However, the packets may themselves be randomly distributed within the turbulent boundary layer.

Recent high-resolution velocity field measurements within the turbulent boundary

layer using particle image velocimetry (Meinhart 1994; Meinhart & Adrian 1995; Meinhart, Adrian & Tomkins 1999) have revealed that the boundary layer is thickly populated with hairpin vortices, which are aligned one behind the other forming coherent packets of hairpin vortices. These vortices were observed to pass low-speed fluid from the downstream vortex to its upstream neighbour and so on over several hairpin vortices to form near-wall low-speed streaks of length significantly longer than the streamwise lengthscale of any single hairpin vortex. This convincingly explains the often observed very long near-wall low-speed streaks. It was observed in these experiments that the outer envelope of the coherent packet of hairpin vortices takes many different shapes. The often observed scenario is a primary hairpin vortex followed by a sequence of younger hairpins on its upstream end. Also observed in some of the flow fields is a sequence of smaller and possibly younger hairpins on the downstream side of the primary hairpin, thus forming a tent-like hairpin packet. At higher Re_θ the hairpin packets were not limited to the near-wall region and their envelopes were distinct from the outer edge of the boundary layer.

Earlier, Bandyopadhyay (1980), based on his experimental observations, presented a phenomenological model of turbulent boundary layer consisting of groups of hairpins. According to this model, the oldest member of the group is the biggest and is located at the downstream end of the hairpin packet. The upstream hairpins are successively younger and smaller and thus the envelope of the group of vortices is tilted upwards in the downstream direction. Based on an estimate for the growth rate of the hairpin vortices and their convective velocity, Bandyopadhyay (1980) predicted the tilt angle of the hairpin packet to be approximately 18°. Based on hydrogen bubble visualizations in a turbulent boundary layer and the resulting bubble pattern in the near-wall region below $y^+ = 100$, Smith (1984) reported the pattern to be consistent with a group of streamwise aligned hairpin vortices. Further, in experiments where the laminar boundary layer is locally disturbed by a small hemispherical bump (Acarlar & Smith 1987*a*), it was observed that a continuous train of vortices was shed downstream of the disturbance. Experiments were also conducted in a laminar boundary layer with an impulsive injection of fluid normal to the boundary (Acarlar & Smith 1987*b*; Haidari & Smith 1994). These experiments demonstrated the possibility of hairpin vortices occurring in groups of fixed spatial arrangement.

Haidari & Smith (1994) have addressed the process of a single hairpin vortex, generated by an initial impulsive injection of fluid, subsequently generating subsidiary vortices to form a packet of hairpin vortices. They interpreted the hydrogen bubble and dye flow visualization results to indicate the formation of new hairpins directly behind and to the sides of the primary mature hairpin vortex, which was generated by the initial injection of fluid. This process of initial hairpin formation from fluid injection and subsequent generation of additional hairpins in a laminar boundary layer was studied numerically by Singer & Joslin (1994). In an earlier experiment Acarlar & Smith (1987*a*) followed the continuous generation of hairpin vortices in a laminar boundary layer behind a hemispherical bump. Here, the bump acts to disturb the flow continuously, resulting in the steady formation of a continuous stream of hairpin vortices. Whereas in the case of an impulsive injection, only the primary hairpin was generated by the injection and the subsequent hairpins were generated from the interaction of the primary hairpin with the wall layer. Thus, unlike the hemispherical bump, impulsive injection of fluid can be considered to address the natural formation of hairpin packets more closely. In support of the above experimental observations, Smith *et al.* (1991) offered an inviscid model to explain the generation of additional hairpins from a single mature hairpin vortex.

Although the above studies have been limited to laminar boundary layers, it seems reasonable to expect that this mechanism is active even in the turbulent regime. This process of hairpin packet formation then needs to be understood in the context of a turbulent boundary layer. Flow visualizations and PIV measurements have provided convincing evidence for the development of a single hairpin into a hairpin packet, but our understanding of the mechanistic details of this process is incomplete. Inviscid models, while they are adequate for describing inviscid processes such as vortex stretching and tilting, do not account for viscous processes such as vortex breakup and vortex reconnection, and therefore do not provide a complete picture.

Recently, using direct numerical simulation of the Navier–Stokes equations, Zhou, Adrian & Balachandar (1996) considered the evolution of a hairpin vortex in a unidirectional mean flow obtained from the low-Reynolds-number turbulent channel flow of Kim, Moin & Moser (1987). The process of autogeneration of new hairpin vortices from a single initial hairpin leading to a hairpin packet was demonstrated. A significant difference between this and the previous efforts is that the initial vortex structure was not generated by a surface mounted disturbance or impulsive injection of fluid. The initial flow structure was a viscous hairpin-like vortex structure extracted from the full two-point correlation tensor of the $Re_\tau = 180$ channel flow database (Kim *et al.* 1987) using the linear stochastic estimation procedure (cf. Adrian 1996). By virtue of being extracted from the correlation tensor, the initial structure has lengthscales, shape and vorticity consistent with the eddies that occur in the fully turbulent channel flow. Studying the evolution of this initial vortex structure in a clean turbulent mean flow environment (i.e. without the complications arising from the presence of other eddies) made it possible to visualize the complex evolution of the initial vortex structure and the subsequent autogeneration of new hairpin vortices.

Here, we extend the previous study, and address in detail the mechanisms responsible for the autogeneration of hairpin vortices. While several aspects of this investigation are similar to the model of Smith *et al.* (1991), the present results will be based on the full viscous solution of the Navier–Stokes equations that began with an estimate of the single vortex structure, which was obtained from the turbulent channel flow DNS database, superposed on a clean unidirectional turbulent mean flow. Particular attention will be paid towards accurately following the self- and mutual-induction and vortex reconnection processes. It is observed that while stronger initial vortices result in the formation of a hairpin packet, weaker initial vortical structures, which live long and maintain their integrity, do not participate in the autogeneration of additional hairpins. Here, criteria for the generation of new hairpins, in terms of the strength and location of the initial hairpin will also be formulated. It is also observed that in addition to the sequence of new hairpins generated on the upstream side, hairpins are also generated on the downstream side of the initial vortex. The characteristic shape of the resulting hairpin packet, its size and spatial dimensions will also be discussed. The instantaneous velocity field corresponding to the hairpin packet will be extracted on a longitudinal vertical plane passing through the centre of the hairpin heads in order to illustrate the striking similarity to the experimental PIV measurements of Meinhart *et al.* 1999).

In addition to the generation of new hairpins upstream and downstream of the primary hairpin vortex, new quasi-streamwise vortices are also observed primarily on the outboard side of the hairpin vortex legs. The detailed mechanism responsible for their formation will be explored and compared with those proposed by Brooke & Hanratty (1993) and Benard, Thomas & Handler (1993). The effect of asymmetry on the evolution of the vortical structures will also be explored. Finally, the present

results will clearly establish the causes and effects and provide a mechanistic picture of the autogeneration process leading to the natural formation of hairpin packets.

The rest of the paper is organized as follows. In § 2, the extraction of the initial structure using stochastic estimation methodology will be discussed first; followed by a brief discussion of the numerical simulation and the vortex identification methodology. Section 3 is broken into ten subsections and the various aspects of the results obtained are presented. The development of the initial structure into a hairpin packet is addressed in §§ 3.1 to 3.5. The growth and threshold behaviour for the autoregeneration process are discussed in § 3.6, followed by comparison of the computed vortical structure with the experimental measurements in § 3.7. Section 3.8 covers the generation of additional quasi-streamwise vortices and in § 3.9 the convective velocity of the hairpin packet is presented. The effect of asymmetry on the evolution of hairpin structures is addressed in § 3.10. Finally, in § 4 summary and conclusions are provided.

2. Methodology

2.1. *Linear stochastic estimation*

The initial vortical structure whose evolution will be followed in detail is obtained from the linear stochastic estimation (LSE) procedure applied to the $Re_\tau = 180$ turbulent-channel-flow two-point correlation database (Kim *et al.* 1987). The extraction of coherent structures in turbulent flows by stochastic estimation has been discussed extensively in the past (Adrian 1996). Here, the linear stochastic estimation procedure is used to obtain the best linear approximation to the conditionally averaged flow field $\langle \boldsymbol{u}'(\boldsymbol{x}')|\boldsymbol{u}(\boldsymbol{x})\rangle$ where $\boldsymbol{u}(\boldsymbol{x})$ is the velocity event specified at the point $\boldsymbol{x}$ upon which the flow is conditioned. This best linear approximation can be evaluated in terms of the unconditional two-point velocity correlation. In linear stochastic estimation, the best linear estimate of the fluctuating flow field, $\hat{u}_i'(\boldsymbol{x}')$, is written in terms of an event vector $u_j(\boldsymbol{x})$ as

$$\hat{u}_i'(\boldsymbol{x}') = \sum_{j=1}^{3} L_{ij}(\boldsymbol{x}', \boldsymbol{x}) u_j, \tag{1}$$

where L_{ij} are the linear estimation coefficients to be determined such that the mean square error between the linear estimate, $\hat{\boldsymbol{u}}'(\boldsymbol{x}')$, and the conditional average, $\langle \boldsymbol{u}'(\boldsymbol{x}')|\boldsymbol{u}(\boldsymbol{x})\rangle$, is minimized. This minimization yields a system of linear equations known as the Yule–Walker equation (see Adrian 1996) for L_{ij} as

$$\sum_{j=1}^{3} \langle u_k u_j \rangle L_{ij} = \langle u_i' u_k \rangle. \tag{2}$$

In the above equation $\langle u_i' u_k \rangle$ and $\langle u_k u_j \rangle$ are two-point correlation between the velocity field and the event vector and among the components of the event vector, respectively. The best linear estimate of the total flow field is

$$\tilde{u}_i'(\boldsymbol{x}') = U_i(y') + \hat{u}_i'(\boldsymbol{x}'), \tag{3}$$

where U_i is the mean velocity of the turbulent flow.

The estimated field depends on the event vector. Because of the crucial role played by second quadrant turbulent events, we consider the symmetric Q2 event vector given by ($u < 0, v > 0$ and $w = 0$) specified at a single point within the channel. The streamwise and wall normal velocity components of the event vector are chosen

based on their contribution to mean Reynolds shear stress, $\overline{uv}$. Moin, Adrian & Kim (1987) lists the values of $u = u_m$ and $v = v_m$ which maximize the product $u_m v_m$ weighted by the probability density of its occurrence $f(u_m, v_m)$ and thereby maximize the contribution to mean Reynolds shear stress.

The choice of a symmetric Q2 event vector results in a vortical structure that resembles a near-wall quasi-streamwise vortex pair when the event is specified close to the wall and resembles a hairpin vortex when the event is specified sufficiently far away from the wall (Moin *et al.* 1987). In the present study, since it is of interest to investigate in detail the evolution and dynamics of these near-wall vortical structures, the wall normal location, y_m^+, of the event vector will be varied from near the boundary to the middle of the channel. Furthermore, it is recognized that the strength of the initial structure can play an important role, especially in the nonlinear stages of the evolution. Therefore, the symmetric event vector is specified as $u = \alpha u_m$, $v = \alpha v_m$ and $w = 0$, where the multiplicative factor α, here referred to as the relative amplitude of the initial structure, is varied from 0.25 to 3.0. The peak non-dimensional vorticity of the initial structure with $\alpha = 1$ is 32.6 and it can be compared to the peak non-dimensional vorticity of 650 for the mean turbulent flow profile at the wall. Owing to the linearity of the stochastic estimation procedure employed, the peak, as well as the average vorticity of the initial vortical structure, scales with α.

In addition to symmetric initial structures, evolution of asymmetric structures is also investigated. Here, an initial asymmetric vortical structure was obtained by specifying an asymmetric event vector as $u = \alpha u_m$, $v = \alpha v_m$ and $w \neq 0$. The evolution of different initial structures with varying magnitude of spanwise velocity is considered. Given a sufficiently strong spanwise component of velocity in the event vector, the level of asymmetry can be made significant.

2.2. *Simulation of the dynamics*

Once the initial vortex structure has been obtained from the linear stochastic estimation procedure, it is superposed on a turbulent mean flow profile evaluated from the $Re_\tau = 180$ direct numerical simulation database (Kim *et al.* 1987) to form the initial flow field whose time evolution is under investigation. Here, this initial flow field is evolved in time by solving the Navier–Stokes equation along with the incompressibility condition written in non-dimensional form as shown below:

$$\nabla \cdot \boldsymbol{u} = 0, \tag{4a}$$

$$\frac{\partial \boldsymbol{u}}{\partial t} + (\boldsymbol{u} \cdot \nabla)\boldsymbol{u} = -\nabla p + \frac{1}{Re_\tau} \nabla \cdot \nabla \boldsymbol{u}. \tag{4b}$$

In the above equation, the channel half-height h is used as the lengthscale. Wall friction velocity $u_\tau \equiv (\nu(\partial \overline{u}/\partial y)|_{y=\pm h})^{1/2}$ is used as the velocity scale, the characteristic pressure and time scales are ρu_τ^2 and h/u_τ, respectively. This scaling results in the only non-dimensional parameter of Reynolds number based on friction velocity, $Re_\tau = u_\tau h/\nu$.

The present simulations were performed at a Reynolds number of $Re_\tau = 180$. The simulations employ periodic boundary conditions along the streamwise (x) and spanwise (z) directions. The sizes of the computational domains along these directions in non-dimensional units are 4π and $\frac{4}{3}\pi$, respectively. See figure 1 for a schematic of the computational domain and coordinate definition. The periodic directions are discretized by a uniformly spaced grid and Fourier expansions are used as part of the spectral collocation methodology. The wall normal direction (y) is non-periodic and

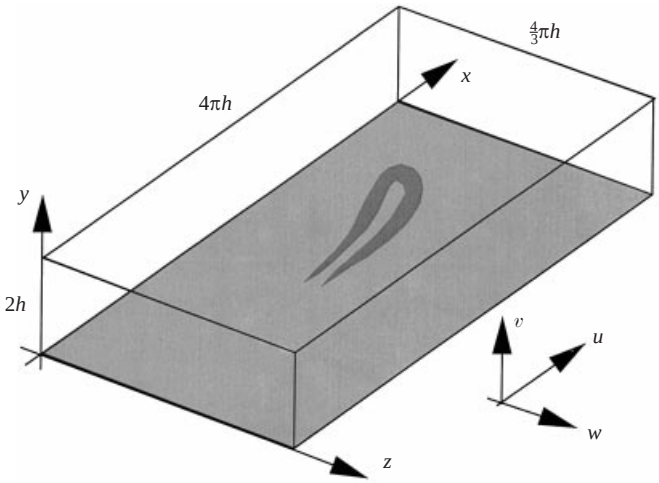

FIGURE 1. Schematic of the computational domain (x, streamwise direction; y, wall normal direction; z, spanwise direction). In viscous wall units the size of the computational box is given by $4\pi h^+ \times 2h^+ \times \frac{4}{3}\pi h^+ = 2262 \times 360 \times 754$.

a Chebyshev expansion is used along this direction with Gauss–Lobatto points for spatial discretization. A typical resolution of $96 \times 97 \times 96$ grid points along the x-, y- and z-directions is used in most of the simulations to be reported, which results in a uniform grid spacing of 23.56 and 7.85 viscous wall units along the streamwise (x) and spanwise (z) directions, respectively. Along the wall normal direction, the grid spacing in viscous wall units varies from 0.096 close to the walls to 5.96 near the centre of the channel. The sufficiency of grid resolution has been verified by comparing the results with those obtained for a few cases on a finer grid resolution of $128 \times 129 \times 128$ points.

Here, we employ the operator or time-splitting technique for the decoupling of the pressure computations in the time advancement of the flow field. In brief, at each timestep, first an intermediate velocity field is computed with only the advection and diffusion effects taken into account. This intermediate velocity field is not divergence free. In the second step, an appropriate pressure is computed by solving a Poisson equation for pressure, based on which a pressure correction is applied to the intermediate velocity field to make it divergence free. Here, we employ a third-order Runge–Kutta scheme for the advection term and an implicit Crank–Nicholson scheme for the diffusion term. The pressure effect is considered to be fully implicit in order to guarantee zero divergence at the end of the full timestep. The details of the numerical procedure used in this channel-flow simulation are considered standard (Kendall 1992) and will not be elaborated here.

2.3. *Vortex identification*

A key aspect of the current study is the identification and tracking of vortical structures: therefore, an accurate vortex extraction method is required. The conceptual notion of a vortex usually refers to a tube-like structure with persistent and coherent rotation about its spine. Although a universally accepted definition of vortex is still lacking, Robinson, Kline & Spalart (1988) proposed the following description: "A vortex exists when instantaneous streamlines mapped onto a plane normal to the vortex core exhibit a roughly circular or spiral pattern, when viewed from a reference

frame moving with the center of the vortex core." This definition makes a clear distinction between a vortex characterized as a structure with a certain topological feature and other mathematically well-defined quantities such as vorticity, helicity, etc. Unfortunately, this description itself requires *a priori* knowledge of the location of the vortex core.

On the other hand, a number of techniques for the identification of vortices have been proposed. These techniques employ the iso-surface of vorticity magnitude, local clustering of vortex lines (Kim *et al.* 1987), elongated regions of low pressure (Robinson *et al.* 1988), regions of complex eigenvalues of the velocity gradient tensor (Chong, Perry & Cantwell 1990; Dallmann *et al.* 1991; Soria & Cantwell 1993), the Hessian of pressure (Jeong & Hussain 1995) and the second invariant of the velocity gradient tensor (Hunt, Wray & Moin 1988; Zhong, Huang & Adrian 1996*b*), as possible candidates for vortex identification. All the above methods are powerful in capturing some signatures of the vortex and have proved successful under certain flow situations, but have their limitations.

Here, we follow Chong *et al.* (1990) in their general classification of the three-dimensional velocity field around a critical point. The local velocity field around a point denoted by the position vector $\boldsymbol{r}$ can be expressed to linear order as

$$\boldsymbol{u}(\boldsymbol{r}+\delta\boldsymbol{r}) = \boldsymbol{u}(\boldsymbol{r}) + \boldsymbol{D}\delta\boldsymbol{r} + O(||\delta\boldsymbol{r}||^2), \tag{5}$$

where $\boldsymbol{D} = \nabla\boldsymbol{u}$ is the velocity gradient tensor. Its characteristic equation is given by

$$\lambda^3 + P\lambda^2 + Q\lambda + R = 0, \tag{6}$$

where $P = -\mathrm{tr}(\boldsymbol{D}) = -\mathrm{div}\,\boldsymbol{u}$, is an invariant of the velocity gradient tensor, which is identically zero for incompressible flows. The other two invariants of $\boldsymbol{D}$ are $Q = \frac{1}{2}\left[P^2 - \mathrm{tr}(\boldsymbol{DD})\right]$, and $R = \frac{1}{3}\left[-P^3 + 3PQ - \mathrm{tr}(\boldsymbol{DDD})\right] = -\det(\boldsymbol{D})$. The discriminant for this characteristic equation is

$$\Delta \equiv \left(\tfrac{1}{2}\tilde{R}\right)^2 + \left(\tfrac{1}{3}\tilde{Q}\right)^3, \tag{7}$$

where $\tilde{R} \equiv R + \frac{2}{27}P^3 - \frac{1}{3}PQ$ and $\tilde{Q} \equiv Q - \frac{1}{3}P^2$. The velocity gradient tensor $\boldsymbol{D}$ has a real eigenvalue and a pair of conjugated complex eigenvalues when the discriminant Δ is positive. Based on the above classification, a number of vortex identification methods have been suggested. Chong *et al.* (1990) proposed the use of the region where an eigenvalue pair is complex to represent a vortex. In practice, it was necessary to combine this methodology with the concentration of vorticity magnitude to obtain a reasonable shape for the vortex.

A similar approach has been proposed by Dallmann *et al.* (1991). Hunt *et al.* (1988) indicated that the second invariant (Q) of the velocity gradient tensor is a quantity that measures the dominance of vorticity over strain and proposed that it could be used as a criterion to identify vortices in two-dimensional turbulent flows. By comparing results obtained from different combinations of the invariants of the velocity gradient tensor, Zhong *et al.* (1996) suggested using contours of the second invariant, in the region where the tensor has complex eigenvalue, to visualize vortices.

In the present study, we prefer to use the imaginary part of the complex eigenvalue of the velocity gradient tensor to visualize vortices. This idea is based on the fact that the velocity gradient tensor $\boldsymbol{D}$ in Cartesian coordinates can be decomposed as,

$$\boldsymbol{D} \equiv \left[d_{ij}\right] = [\boldsymbol{v}_r \;\; \boldsymbol{v}_{cr} \;\; \boldsymbol{v}_{ci}] \begin{bmatrix} \lambda_r & & \\ & \lambda_{cr} & \lambda_{ci} \\ & -\lambda_{ci} & \lambda_{cr} \end{bmatrix} [\boldsymbol{v}_r \;\; \boldsymbol{v}_{cr} \;\; \boldsymbol{v}_{ci}]^{-1}, \tag{8}$$

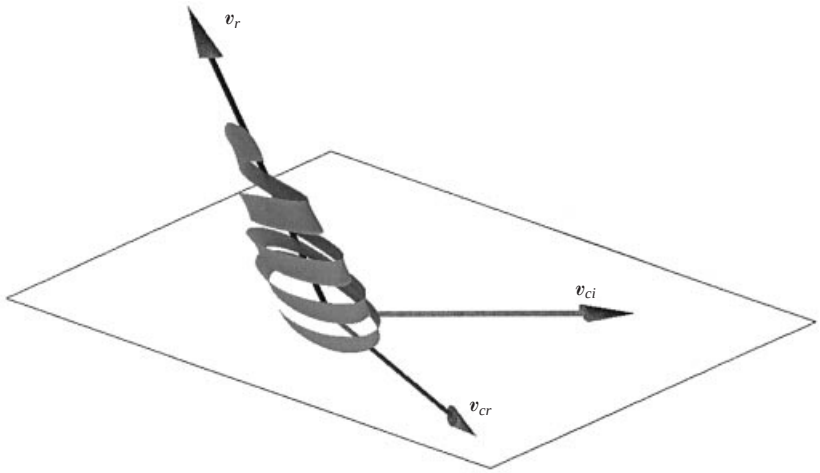

FIGURE 2. The local streamline pattern with the eigenvectors of the velocity gradient tensor in the neighbourhood of a vortex core.

where λ_r is the real eigenvalue with a corresponding eigenvector $\boldsymbol{v}_r$, and $\lambda_{cr} \pm \lambda_{ci}i$ are the conjugate pair of the complex eigenvalues with complex eigenvectors $\boldsymbol{v}_{cr} \pm \boldsymbol{v}_{ci}i$. In a local (curvilinear) coordinate (y_1, y_2, y_3) system defined by the three vectors $\{\boldsymbol{v}_r, \boldsymbol{v}_{cr}, \boldsymbol{v}_{ci}\}$, the local streamlines can then be expressed as

$$y_1(t) = C_r \exp \lambda_r t, \tag{9a}$$

$$y_2(t) = \exp \lambda_{cr} t [C_c^{(1)} \cos(\lambda_{ci} t) + C_c^{(2)} \sin(\lambda_{ci} t)], \tag{9b}$$

$$y_2(t) = \exp \lambda_{cr} t \left[C_c^{(2)} \cos(\lambda_{ci} t) - C_c^{(1)} \sin(\lambda_{ci} t)\right], \tag{9c}$$

where $C_r, C_c^{(1)}$, and $C_c^{(2)}$ are constants. Therefore, as shown in figure 2, the local flow is either stretched or compressed along the axis $\boldsymbol{v}_r$, while on the plane spanned by the vectors $\boldsymbol{v}_{cr}$ and $\boldsymbol{v}_{ci}$, the flow is swirling. Moreover, the strength of the local swirling motion is quantified by λ_{ci}, and thus, in the present report, the imaginary part of the complex eigenvalue pair will be referred to as the local *swirling strength* of the vortex.

We have used the isosurfaces of the imaginary part of the eigenvalue to visualize vortices in the present study. There are several advantages of this method. First, this method is frame independent, eliminating the difficulty of choosing a proper frame of reference. Secondly, only in regions of local circular or spiralling streamline is the eigenvalue complex, so, this method automatically eliminates regions having vorticity but no local spiralling motion, such as shear layers. In particular, the vortical structures are extracted by plotting isosurfaces of λ_{ci}^2 equal to some threshold. The term λ_{ci}^2 is analogous to enstrophy, and it is also dimensionally consistent with other quantities such as Q used previously in the identification of vortices. Although, from theoretical grounds, this threshold can be chosen to be zero, the surface with a positive threshold (which can be set at a few percent of the maximum value) appears significantly smoother, allowing easy interpretation. Figures 3(*a*), 3(*b*) and 3(*c*) show a complex pattern of near-wall vortical structures visualized with three different thresholds of 1.4%, 2.8% and 4.2% of the maximum value of 720. It can be seen that the general topology of the visualized vortical structure remains nearly the same, independent of the amplitude chosen for visualization. Characteristic information,

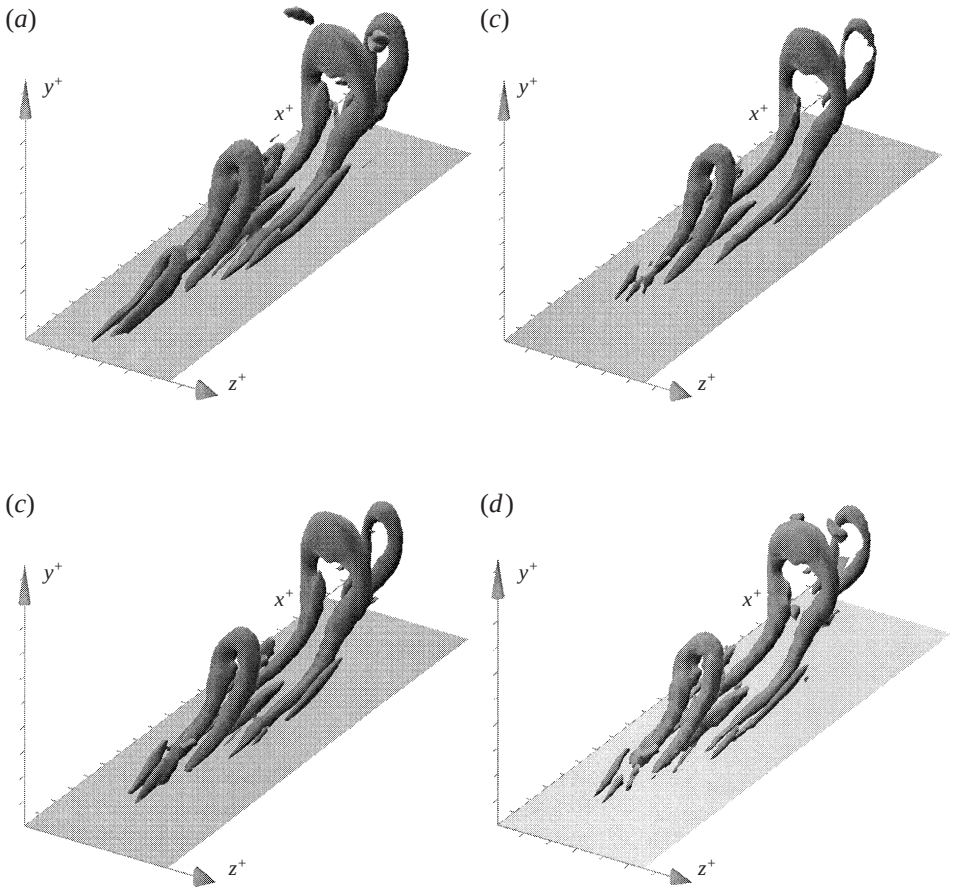

FIGURE 3. Vortical structures identified by an iso-surface of (*a*) λ_{ci}^2 with 1.4% of maximum; (*b*) λ_{ci}^2 with 2.8% of maximum; (*c*) λ_{ci}^2 with 4.2% of maximum; (*d*) $\lambda_2 = -10$ (see Jeong & Hussain 1995).

such as the tilt angle of the vortex legs, tilt angle of the hairpin heads, spanwise distance between the quasi-streamwise vortex legs, streamwise separation between the different hairpin heads, remain invariant. However as the amplitude of visualization is increased, the diameter and the length of the vortical structures can be observed to decrease somewhat. Each one of the vortical structures to be presented in this paper was visualized with a wide range of threshold amplitude using an automated three-dimensional graphical tool. The choice of λ_{ci}^2 for presentation was made so that the various vortical structures would be easily identifiable with minimal background noise, and that the interpretations and final conclusions to be drawn were not sensitively dependent on this choice of value.

Finally, it must also be pointed out that we have chosen this vortex identification methodology over others mainly because it has been observed to yield a regular and identifiable vortex structure in the present problem consistently under various conditions. We have also used the vortex identification methods proposed by Zhong *et al.* (1996) and Jeong & Hussain (1995). These methods yield qualitatively identical and quantitatively similar results. For example, the near-wall vortices identified based on the eigenvalues of the Hessian of pressure have been plotted in figure 3(*d*). By comparing this with figures 3(*a*)–3(*c*), it is evident that both methods extract very

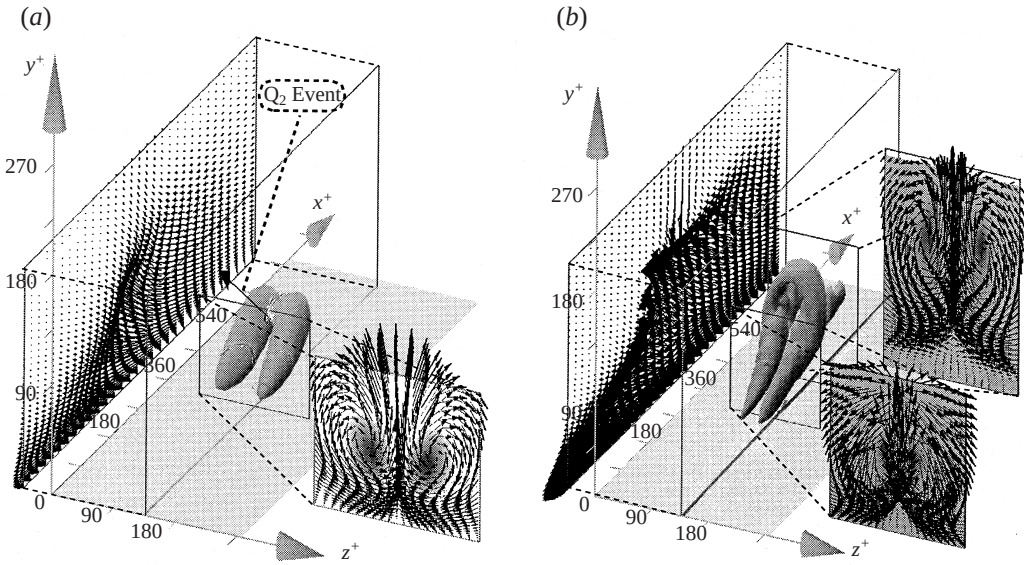

FIGURE 4. Formation of the primary hairpin vortex from an initial vortical structure extracted by an event vector of strength $\alpha = 3.0$ specified at $y_m^+ = 49$. The three-dimensional structures represent iso-surfaces of λ_{ci}^2 equal to 10% of its maximum. Only a section of the entire computational domain surrounding the structures is shown. In order to better visualize the hairpin, the y-direction has been scaled up by a factor of two. The vector plots show in-plane perturbation velocities. The (x, y)-cross-sections are located on the middle of the computational domain and they cut through the hairpin head. (*a*) $t^+ = 0$; the (z, y)-cross-section is at $x^+ = 342$. (*b*) $t^+ = 27$; the (z, y)-cross-sections are at $x^+ = 324$ and 450, respectively.

similar vortical structures. The conclusions to be drawn on the dynamics of the near-wall vortical structures are not affected by the choice of methodology, and therefore we have not pursued here a detailed comparison of the different vortex identification methodologies.

3. Results

3.1. *Initial structure and formation of primary hairpin*

The development and dynamics of vortical structures resulting from symmetric Q2 events are considered first. The initial stochastically estimated structure evolves rapidly into a hairpin-like vortical structure, and this process of initial development is relatively independent of the initial strength (α) and initial location (y_m^+) of the event vector. We have varied the initial strength from $\alpha = 0.25$ to $\alpha = 3.0$ and the initial location from $y_m^+ = 19.2$ to $y_m^+ = 103$, and in each case the initial stochastically estimated structure evolves into a qualitatively similar hairpin vortex during the early phase of evolution. Of course, the strength of the hairpin vortex relative to the mean flow depends on both α and y_m^+, and therefore these two parameters control the subsequent development of the hairpin structure. In this section, we will concentrate on the character of the initial structure and its rapid development into a hairpin vortex, which will be referred to as the primary hairpin vortex (PHV).

A typical velocity field determined by LSE given a Q2 event contains a pair of inclined counter-rotating quasi-streamwise vortices located on either side of the given event vector, such that fluid is pumped up and backwards ($u < 0$ and $v > 0$)

between the streamwise vortices. Figure 4(*a*) shows the tilted streamwise vortex pair associated with an initial Q2 event vector $\boldsymbol{u} = [8.16, 3.54, 0.0]$ corresponding to $\alpha = 3.0$ specified at $y_m^+ = 49.6$. Owing to the linear nature of the estimation procedure, the entire velocity field of the initial structure simply scales linearly with α. The vortex identification method used in figure 4(*a*) is the isosurface of λ_{ci}^2 equal to 57 (8% of the maximum 715). Plotted in this figure are two velocity vector plots: the first on an (x, y)-plane passing between the two legs of the inclined vortex and the second on a (y, z)-plane cutting through the two legs of the vortical structure. Also shown in the (y, z)-plane are the shaded contours of λ_{ci}^2 to better illustrate the location of vortex legs above the wall. The vector plots show perturbation in-plane velocity components, i.e. the mean turbulent streamwise velocity has been subtracted. The strong upward pumping of the fluid between the two legs of the vortex structure and its Q2 nature can be clearly observed in these vector plots.

The quasi-streamwise vortices are about 200 viscous wall units long in the streamwise direction and their ends lie at $y^+ = 12$ at the upstream end and at $y^+ = 65$ at the downstream end, giving them an approximate average inclination of about 15° with respect to the horizontal direction. A closer look reveals that the upstream section of the quasi-streamwise vortices of about 140 viscous wall units length has a shallow inclination of only about 8°, while the downstream end of about 60 viscous wall units has a somewhat steeper inclination of about 25° (for a schematic of the side view see figure 14(*a*)). These, as well as all other geometric data to be reported, are based on an algorithm that extracts the backbone of the vortical structures. Along the spanwise direction, the centres of the streamwise vortex pair are separated by about 40 viscous wall units near the downstream end and by about 100 viscous wall units near the upstream end, thus giving the vortex pair a characteristic Λ shape. The average inclination of the initial structure decreases (or increases) as the y-location of the event vector is lowered (or raised), but the spanwise separation at the upstream end remains at about 100 viscous wall units approximately independent of y_m^+. This is consistent with the accepted mean low-speed streak spacing of about 100 viscous wall units in the near-wall region.

In figure 4(*a*), the two streamwise vortices can be seen to be connected at the downstream end by a narrow bridge. Along the vortices, the peak vorticity component normal to the spanwise direction (or the quasi-streamwise component of vorticity) occurs near this bridge. The non-dimensional value of the streamwise and wall normal vorticity components (non-dimensionalized by u_τ/h) at this location of maximum strength are approximately 42 and 51.5, corresponding to a vortex vector angle of about 50°. This is significantly larger than the local inclination of the vortical structure of 25°. This observation is true over almost the entire length of the quasi-streamwise vortex. Bernard *et al.* (1993) have also observed that the local vorticity vector is more inclined than the vortex structure itself in their DNS result of channel flow. This suggests a possible drawback of vortex identification based on vortex lines. This point has also been addressed by Robinson (1991, 1993). A detailed local investigation reveals that this narrow bridge is primarily made up of spanwise vorticity whose maximum magnitude is approximately 35 in non-dimensional units. The location of the spanwise bridge is slightly upstream of the downstream tip of the quasi-streamwise vortices. In other words, the quasi-streamwise vortices extend slightly beyond their spanwise bridge. This feature of the initial vortical structure will later be shown to play an important role in the generation of new downstream vortical structures. The spanwise bridge becomes stronger as the location of the event vector, y_m^+, increases and the initial structure resembles more closely a hairpin vortex. For a detailed

characterization of the initial structure corresponding to various y_m^+ locations, the reader is referred to Kendall (1992) and Adrian, Moin & Moser (1987).

The initial structure shown in figure 4(*a*) quickly evolves into a hairpin-like vortex as shown in figure 4(*b*) at a non-dimensional viscous time unit of $t^+ = 27$. This figure, like figure 4(*a*), shows only a section of the computational domain surrounding the vortical structure. During this period the centre of the vortex structure moves 377 viscous wall units along the streamwise direction. Also shown in this figure are the velocity vectors on one (x, y)-plane passing between the quasi-streamwise legs and two (y, z)-planes cutting through the quasi-streamwise legs. The geometry of the vortex resembles in appearance the instantaneous hairpin vortex structure observed in experiments and computations (see Head & Bandyopadhay 1981; Robinson 1991; Haidari & Smith 1994). In the perspective view, in addition to the hairpin vortex, a pair of vortical tongues can be seen to stick out at the downstream end of the hairpin vortex, which will be discussed below.

The development of this hairpin structure from its initial form shown in figure 4(*a*) is through a series of distinct and characteristic events. First, the quasi-streamwise vortices lift away from the boundary, which can be explained as the effect of induced velocity of one vortex leg on the other in accordance to the Biot–Savart law. Since the spanwise distance between the quasi-streamwise vortex pair is shorter near the downstream end, the mutual induction is stronger there, and therefore the downstream end of the vortex pair lifts up more rapidly than the upstream end. This lift-up of the downstream portion is particularly strong where the quasi-streamwise vortices are connected by the narrow spanwise bridge, since there the local vortex strength is at its maximum and the spanwise separation is at its minimum. Furthermore, the lift-up process is somewhat mitigated at the upstream end by the strong stretching due to the shear associated with the mean flow gradient, which is most active near the boundaries.

The resulting intermediate structure is curved upwards with the vortex tilt towards the vertical direction increasing downstream from the upstream end. This vortical structure (shown in figure 4*b*) can be reasonably approximated to be made up of two segments: an upstream section of length 125 viscous wall units at an inclination of approximately 17° to the horizontal; and a downstream section of 25 viscous units in streamwise extent with a steep inclination of approximately 75°. Thus, the total streamwise extent of the vortical structure at $t^+ = 27$ has decreased to approximately 150 viscous wall units. During this period the length of the vortical structure, along its backbone, has slightly increased, but owing to the steep 75° inclination of the hairpin structure near its head, the streamwise extent has decreased. This curling-up of the initial quasi-streamwise vortices into a hairpin structure is due to the competing effects of self-induced velocity of the vortical structure on itself and the shear induced stretching due to the background mean turbulent profile. This curl-up process can be followed in the side view of the channel shown in figure 5. In figure 5(*a*), the shaded region is the side view of the three-dimensional vortical structure identified by an isosurface of λ_{ci}^2 equal to 8% of the maximum value at $t^+ = 9$. To help visualize these vortical structures, their backbones are sketched in the figure as a thick dark line. Even at this early time during the formation of the hairpin vortex, the beginning of the curl-up can be identified. Also, the side view of the downstream vortex tongues, which extend almost parallel to the x-axis, can be seen.

The quasi-streamwise vortices pump fluid up and back, away from the boundary in between them, owing to their Q2 nature. This induced back flow encounters the mean flow and forms a shear layer, which is most visible in the vertical plane passing

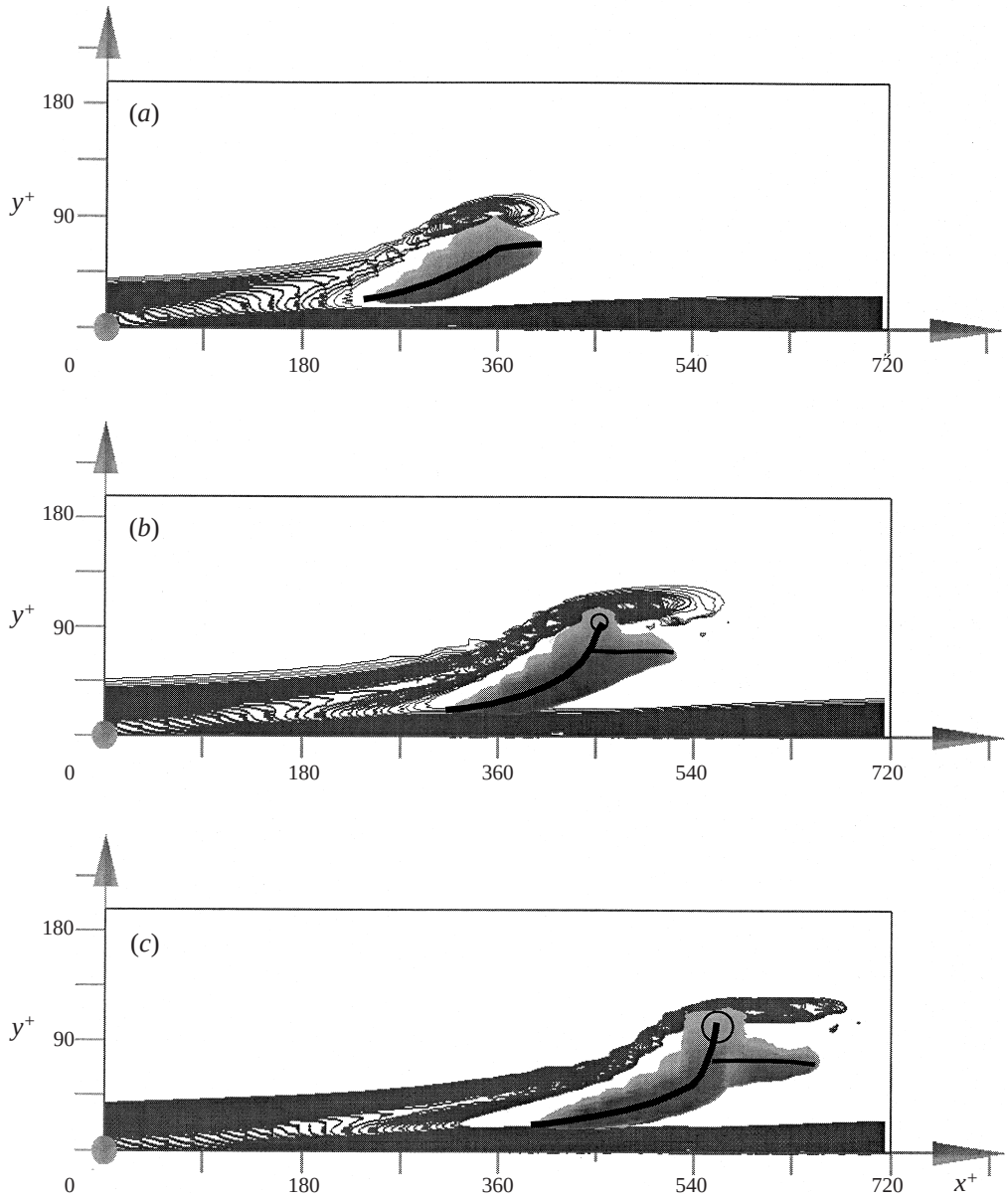

FIGURE 5. Side view of vortex structure identified by λ_{ci}^2. Also identified is the corresponding shear layer in terms of contours of $(-\omega_z)$ on the (x, y) symmetry plane: (*a*) $t^+ = 9$; (*b*) $t^+ = 18$; (*c*) $t^+ = 27$. The initial condition is the same as in figure 4.

between the quasi-streamwise vortex pair. Therefore, also plotted in figure 5 are contours of spanwise vorticity on the (x, y)-midplane. A shear layer can be seen to be located just above the vortex structure. The spanwise separation between the quasi-streamwise vortex pair is at its minimum near the downstream end. This is also the region where the quasi-streamwise vortices are at their peak strength. Therefore, the shear layer is the most intense near the downstream end of the quasi-streamwise vortices. Evolution of the vortical structure and the associated shear layer at $t^+ = 18$

is captured in the side view shown in figure 5(*b*). The quasi-streamwise vortices have curled-up further, the vortical tongues have extended further along the downstream direction and the shear layer has further intensified, particularly near the top of the quasi-streamwise vortices. Local spanwise vorticity associated with the shear layer quickly rolls up in this region and forms a compact spanwise vortex located between the downstream end of the quasi-streamwise vortices. Very quickly, by $t^+ = 27$, the rolled-up spanwise vortex further intensifies and lifts the quasi-streamwise vortices close to it. Viscous vortex connection occurs and the newly rolled-up spanwise vortex connects with the quasi-streamwise vortices to form a hairpin-like vortex structure which can be seen in figure 4(*b*). This process can also be seen in the (x, y)-projection at $t^+ = 27$ shown in figure 5(*c*). Clearly, the spanwise section of the hairpin vortex head is associated with the rolled-up shear layer. The nearly horizontal section of the vortical tongue grows further in the downstream direction.

At this stage, the length of the downstream pair of streamwise vortical tongues is approximately 100 viscous wall units. Although the upstream and downstream ends of the hairpin vortex are now at approximate elevations of 19 and 102 viscous wall units, the upstream end of the hairpin vortex still maintains the characteristic tilt of about 15°. The nearly horizontal downstream vortex pair has a very weak upward tilt of a few degrees, and it is at an approximate elevation of about 70 viscous wall units from the bottom boundary. The spanwise separation between the legs of the hairpin vortex is about 100 viscous wall units near its upstream end, and it is about 40 viscous wall units near the downstream vortical tongues.

This evolution of the initial structure into a hairpin vortex is qualitatively independent of the initial amplitude or the initial location of the event vector. As the strength of the initial event vector (α) is changed, the initial structure always rolls-up into a hairpin vortex, but its strength and accordingly its subsequent evolution differs. As the initial location of the event vector is changed, the main effect is on the length of the resulting hairpin vortex along the streamwise direction, which changes somewhat owing to changes in the delicate balance between the curl-up process due to self-induction and streamwise stretching due to the mean shear, with distance from the wall. Nevertheless the formation process of the primary hairpin vortex remains the same qualitatively. This formation process for a different initial structure with an event vector of slightly lower strength $\alpha = 2.0$, given by $u_i = [7.78, 1.78, 0.0]$, and located closer to the wall at $y_m^+ = 30.3$ is shown in figures 6(*a*) to 6(*c*), corresponding to time instances $t^+ = 54, 72$ and 90. The lift-up of the quasi-streamwise vortices, formation of the shear layer, its roll-up into a spanwise vortex which bridges the two quasi-streamwise legs, and the viscous vortex reconnection to form the hairpin vortex, all take place in this case as well, as is evident from the three frames of figure 6. In particular, the manner in which the downstream pair of vortical tongues are connected to the hairpin vortex can be clearly seen in this case. Their relation can also be better observed in side view, shown in figure 6(*d*) at $t^+ = 90$. Owing to the lower initial strength of the vortical structure and its initial proximity to the wall, the formation of the primary hairpin vortex is somewhat slower than the previous case shown in figures 4 and 5. Also in figure 6, the quasi-streamwise legs of the hairpin structure can be observed to be significantly longer, because of the relative dominance of the mean shear over self-induction in this case.

The presence of a pair of nearly horizontal downstream vortical extensions to the hairpin vortex seen in the above two cases is unexplained, since such vortical structures have not been reported in the past in the context of turbulent boundary layers. It must first be pointed out that these vortical structures were observed in all other

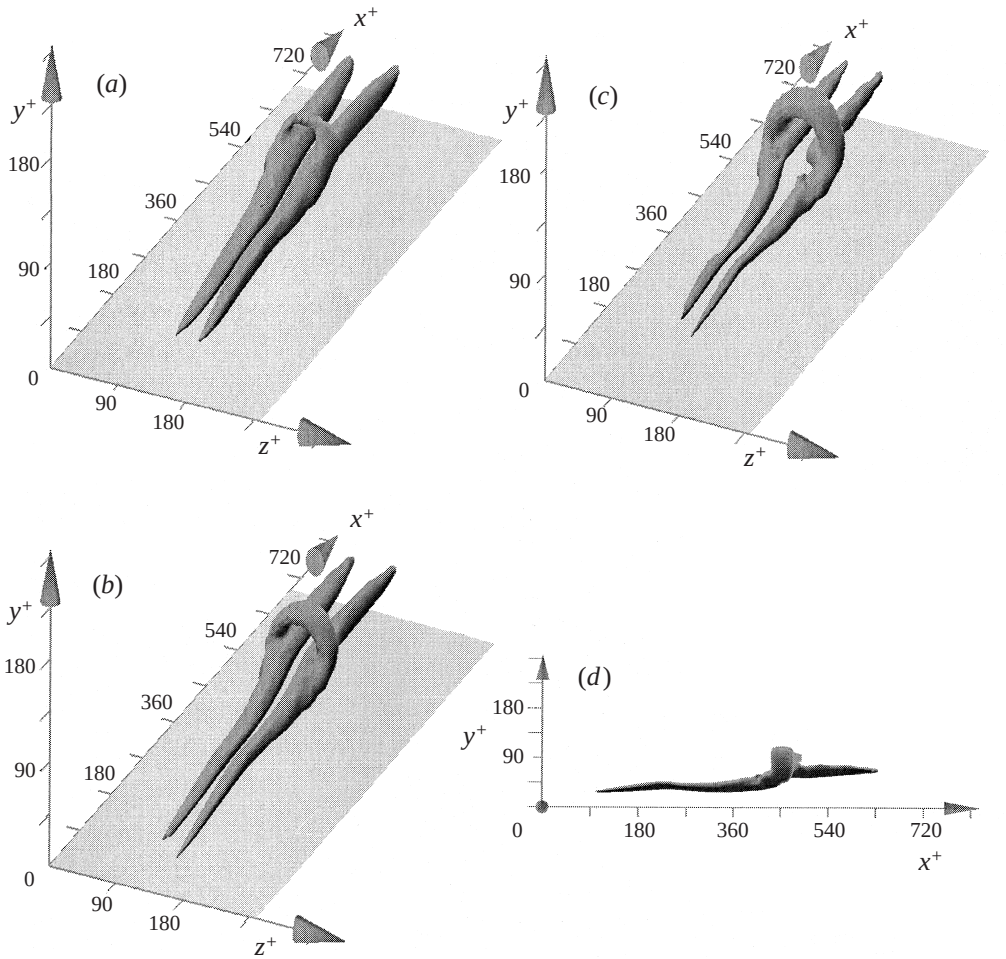

FIGURE 6. Formation of a primary hairpin-like vortex from an initial vortex structure extracted by an event vector of strength $\alpha = 2.0$ specified at $y_m^+ = 30.3$. The three-dimensional structures are identified by iso-surfaces of λ_{ci}^2 equal to 10% of its maximum at (*a*) $t^+ = 54$; (*b*) $t^* = 72$; (*c*) $t^* = 90$; (*d*) the side view at $t^* = 90$.

cases considered in this study as well. The origin of these structures can be traced back to the initial flow field obtained from stochastic estimation. In figure 4(*a*), they can be observed as the tiny downstream extension in the quasi-streamwise vortices beyond the point where they appear to be bridged. While the upstream portion of the initial quasi-streamwise vortices along with the spanwise bridge grows into the hairpin vortex, the small downstream section develops into the long near-horizontal downstream vortical extensions.

This dependence of the vortical tongues on a small feature of the initial condition raises the following question: are these vortical tongues a characteristic feature of the hairpin vortices seen in wall-bounded turbulent flows, or are they artifacts of the initial condition? The initial structures employed in the present study are not arbitrary; they were obtained from the two-point correlation of the turbulent channel flow DNS database, and they represent the best linear approximation to the conditionally averaged flow field consistent with the event vector. Thus, there is reason to believe

that the downstream extensions observed in the initial structure and their subsequent growth into the near-horizontal vortical tongues are characteristic features of wall turbulence. In further support, in the subsequent sections it will be pointed out that as the primary hairpin vortex generates new secondary and tertiary hairpin vortices, vortical tongues are observed to form downstream of these naturally formed hairpin vortices as well. Furthermore, experimental support for the presence of such nearly horizontal downstream extensions to the hairpin vortices comes from the dye visualizations on the generation and downstream evolution of hairpin vortices by Haidari & Smith (1994). Their experimental observations clearly suggest the presence of nearly horizontal downstream vortical extension, in addition to the standard hairpin structure. The flow visualizations shown in their figures 1, 4 and 8 very closely resemble the side view of the vortical structures shown in figures 5(*c*) and 6(*d*). Thus, with reasonable confidence, it can be anticipated that these downstream vortical extensions are a realistic part of near-wall turbulent structures. The importance of these downstream vortical extensions in the generation of new hairpin vortices downstream of the primary hairpin vortex will be explored below.

3.2. *Formation of* Ω*-shaped vortex*

In this section, we will follow the evolution of the primary hairpin vortex shown in figure 4. The primary hairpin vortex, once formed, quickly evolves into the characteristic Ω-shaped vortex shown in figures 7(*a*), 7(*b*) and 7(*c*), corresponding to $t^+ = 36$, 45 and 54, respectively. The head of the vortex continues to lift and tilt upwards into an almost vertical orientation by $t^+ = 54$. In doing so, it also grows wider in the spanwise direction. At $t^+ = 54$, the primary vortex structure can be approximately divided into three segments, as can be seen in the side view shown in figure 7(*d*). The upstream segment is the closest to the bottom boundary and is tilted up from $y^+ = 15$ at its upstream end to $y^+ = 45$. This segment is approximately 180 viscous wall units long and has an inclination of approximately 8°. The spanwise spacing between the vortex legs at the upstream end is approximately 100 viscous wall units.

The middle section of the vortex structure has a very weak negative tilt of approximately −2°. This section is approximately 140 viscous wall units long and is approximately located at $y^+ = 45$. The third section is the head of the vortex structure, which is tilted approximately 75° to the horizontal. Because of this near-vertical orientation, the streamwise extent of this section is only 30 viscous wall units. The near-vertical orientation is due to the backward self-induced motion of the upper portion of the head coupled with little or no forward stretching from the mean shear, which is small in the neighbourhood of the head. The spanwise separation between the the two legs is at its minimum of 30 viscous units where the upstream and middle sections of the vortex structure connect. The spanwise separation is about 40 viscous units where the head connects with the middle section. Owing to the characteristic Ω-shape, the spanwise size of the head is approximately 100 viscous wall units.

Similar Ω-shaped vortices have been reported earlier based on inviscid vortex line calculations (Moin, Leonard & Kim 1986; Kim 1987; Kempka 1988; Hon & Walker 1991). The inviscid simulations of the hairpin-like vortex filaments have shown that the evolution of the vortex into an Ω-shape is due to self-induction. However, unlike the inviscid computations, the present viscous simulations show no tendency for the head of the Ω-shaped vortex to pinch off to form a ring vortex. Kim (1987) computed the evolution of an eddy whose initial field was found by conditional averaging conditioned upon a Q2 event, not unlike the present case. Our results agree well with

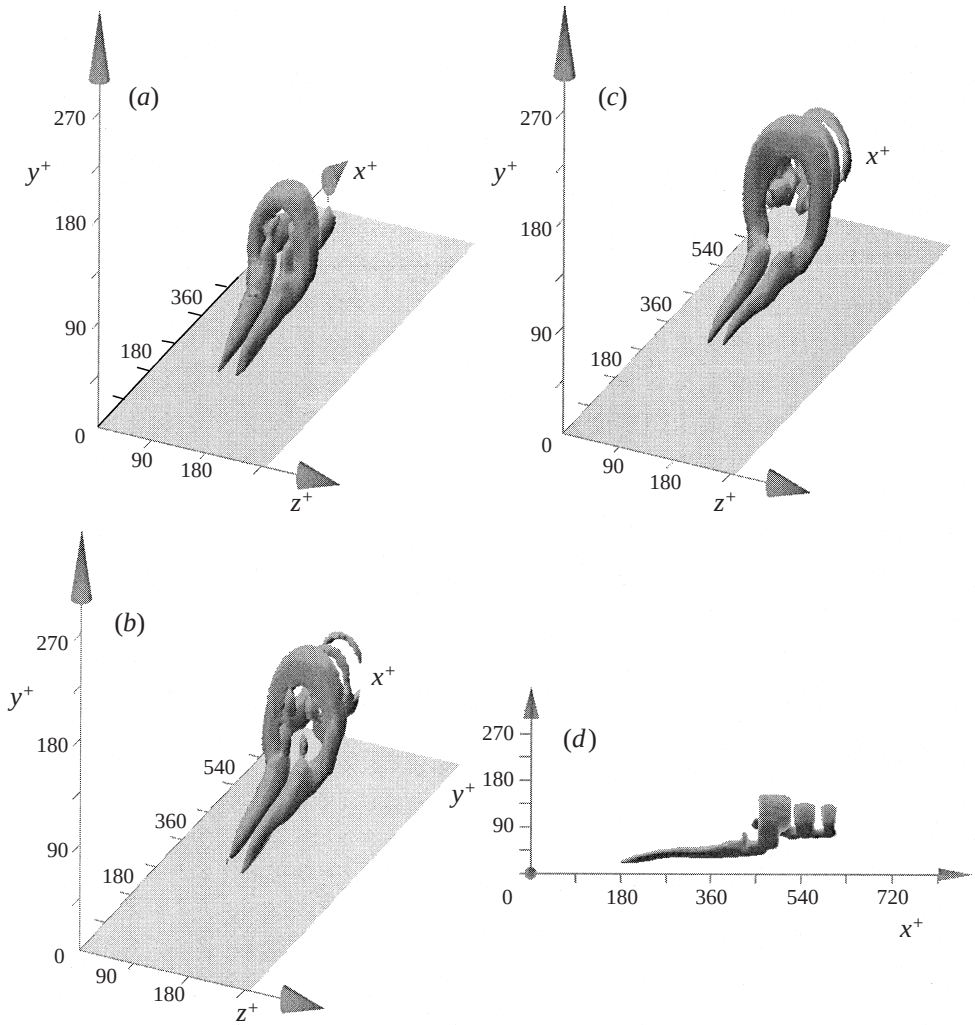

FIGURE 7. Development of the Ω-shaped head following the formation of the primary hairpin vortex shown in figure 4(*b*). Plotted are the iso-surfaces of λ_{ci}^2 equal to 10% of the maximum at (*a*) $t^+ = 36$; (*b*) $t^+ = 45$; (*c*) $t^+ = 54$; (*d*) the side view at $t^+ = 54$.

his. The general agreement of all these calculations indicates that the formation of the Ω-shape is not sensitive to the details of the initial field.

3.3. *Vortex dynamical considerations*

The primary motive in describing near-wall turbulence in terms of vortical structures is to be able to follow their dynamics and delineate causes and effects, based on simple vortex dynamics. Here, we will attempt to explain the details of the formation of the Ω-shaped vortex and its subsequent deformation and evolution based on Biot-Savart law, which for an incompressible flow can be written as:

$$\boldsymbol{u}(\boldsymbol{x}) = -\frac{1}{4\pi}\iiint \frac{(\boldsymbol{x}-\boldsymbol{x}')\times\boldsymbol{\omega}(\boldsymbol{x}')}{|\boldsymbol{x}-\boldsymbol{x}'|^3}\mathrm{d}V(\boldsymbol{x}') + \text{potential flow.} \tag{10}$$

The first term on the right-hand side provides an expression for the velocity $\boldsymbol{u}(\boldsymbol{x})$

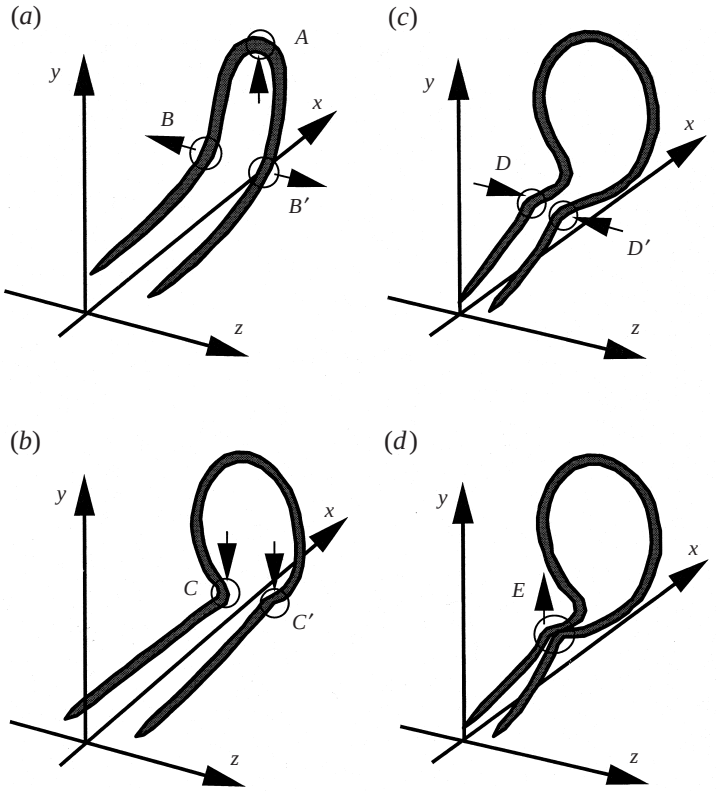

FIGURE 8. Schematic diagrams of the self-induced motion of a hairpin vortex. (*a*) Lifting and broadening of the head; (*b*) formation of the Ω-shaped head and the subsequent downward motion; (*c*) formation of kinks in the hairpin vortex legs and their approach towards each other; (*d*) lifting of the kinks.

in terms of the vorticity distribution $\boldsymbol{\omega}(\boldsymbol{x}')$. With an assumption that the vorticity distribution is only due to an isolated, thin, and elongated vortex tube, the integration can be divided into a local contribution and a non-local contribution coming from $|\boldsymbol{x}-\boldsymbol{x}'| \gg \sigma$, where σ is the thickness of the vortex core. The local effect to the leading order is (Batchelor 1967)

$$K_C \frac{\Gamma}{4\pi} \left(\frac{\partial \boldsymbol{x}}{\partial s} \times \frac{\partial^2 \boldsymbol{x}}{\partial s^2} \right), \tag{11}$$

where s is the arclength along the space curve C that defines the spine of the vortex tube, Γ is the local circulation of the vortex and K_c is a constant whose value depends on the distribution of vorticity within the vortex core. Here $(\partial \boldsymbol{x}/\partial s) \times (\partial^2 \boldsymbol{x}/\partial s^2) = \kappa \boldsymbol{b}$, where κ and $\boldsymbol{b}$ are local curvature and local bi-normal vector of curve C, respectively. Thus, when local curvature is large, the self-induced velocity of the vortex tube is dominated by the local effect, and to leading order the induced motion is in the local bi-normal direction, and it is proportional to both the vortex strength and the local curvature.

A schematic of the formation of the Ω-shaped vortex and its subsequent evolution is shown in figures 8(*a*) to 8(*d*). The initial hairpin vortex in figure 8(*a*) consists of a pair of quasi-streamwise vortices connected at the downstream end by the hairpin head. As pointed out in the previous sections, while the upstream end of the hairpin

vortex is only weakly inclined, the downstream section is tilted up significantly. This results in strong local curvature, primarily in the (x, y)-plane, along the two quasi-streamwise legs at points marked B and B' in figure 8(a). The proper direction of the induced motion due to local curvature is given by the cross-product of the local vorticity vector with the unit vector along the local radius of curvature. The resulting self-induced motion is in the spanwise direction, and it moves the two legs of the hairpin vortex apart, as indicated by the arrows in figure 8(a). This spanwise motion is strong where the vortex is strong and its local curvature is large. The bottom wall, whose effect can be accounted for through an image hairpin vortex, somewhat mitigates this spanwise motion. The effect of the image vortex is to bring the two legs close together. Since the effect of the image vortex is stronger closer to the boundary, the self-induced spanwise spreading reaches its peak away from the boundary, giving the hairpin vortex head its characteristic Ω-shape, as shown in figure 8(b).

The hairpin is strongly curved at its head (marked A in figure 8a). Here, the vorticity is directed along the $-z$-direction and the unit vector along the radius of curvature lies on the (x, y)-plane and its angle to the x-axis varies from about -160° to -100° as the hairpin vortex tilts up. The self-induced motion is therefore pointed up and backward, resulting in further curl-up of the hairpin vortex. In the initial stages, when the downstream section of the quasi-streamwise vortices and their spanwise bridge are inclined at a shallow angle, the induced motion is dominantly to lift up the vortex head. In contrast, towards the later stages, when the hairpin vortex is tilted-up to a near-vertical position, the self-induced motion moves the vortex head backward. Of course, the streamwise stretching of the vortex structure due to the background turbulent mean flow must also be taken into consideration. The effect is most active close to the top and bottom boundaries and progressively decreases towards the interior of the channel.

3.4. *Generation of secondary and tertiary vortices*

The above arguments based on vortex curvature and induced motion can be continued to further follow the evolution of the Ω vortex. As a result of the spanwise broadening of the hairpin vortex into the Ω shape, the primary curvature of the vortex structure in the neck region, where the head connects with the legs (marked C and C' in figure 8b), is in the (x, z)-plane. The vorticity and the normal vectors are locally such that the local self-induced motion at both these points is directed downwards and the neck region moves towards the wall. While the neck region moves down owing to local curvature effect, the rest of the quasi-streamwise vortex legs continues to lift up owing to mutual induction. A diagram of the resulting structure is shown in figure 8(c). As described in figure 7(d), the vortex structure is now made up of three segments: an upstream segment with a small upward tilt; a middle segment with a very weak negative tilt; and a near-vertical Ω-shaped vortex head. As a result, the quasi-streamwise vortex legs acquire a curvature primarily in the (x, y)-plane, where the upstream and middle segments meet (these points are marked D and D' figure 8c). However, since now the curvature is concave downwards, the resulting self-induced spanwise motion pushes the two streamwise vortex legs closer together, particularly where the curvature in the (x, y)-plane is the largest, as shown by arrows in figure 8(c). In turn, the approach of the streamwise legs toward each other increases their mutual induction and results in strong local lift-up. This further increases the local (x, y)-curvature and the self-induced motion of the vortices towards each other. This feedback process evolves rapidly and results in a kink (or a rapid change in the slope) in the long legs of the vortex structure near the junction of the upstream and

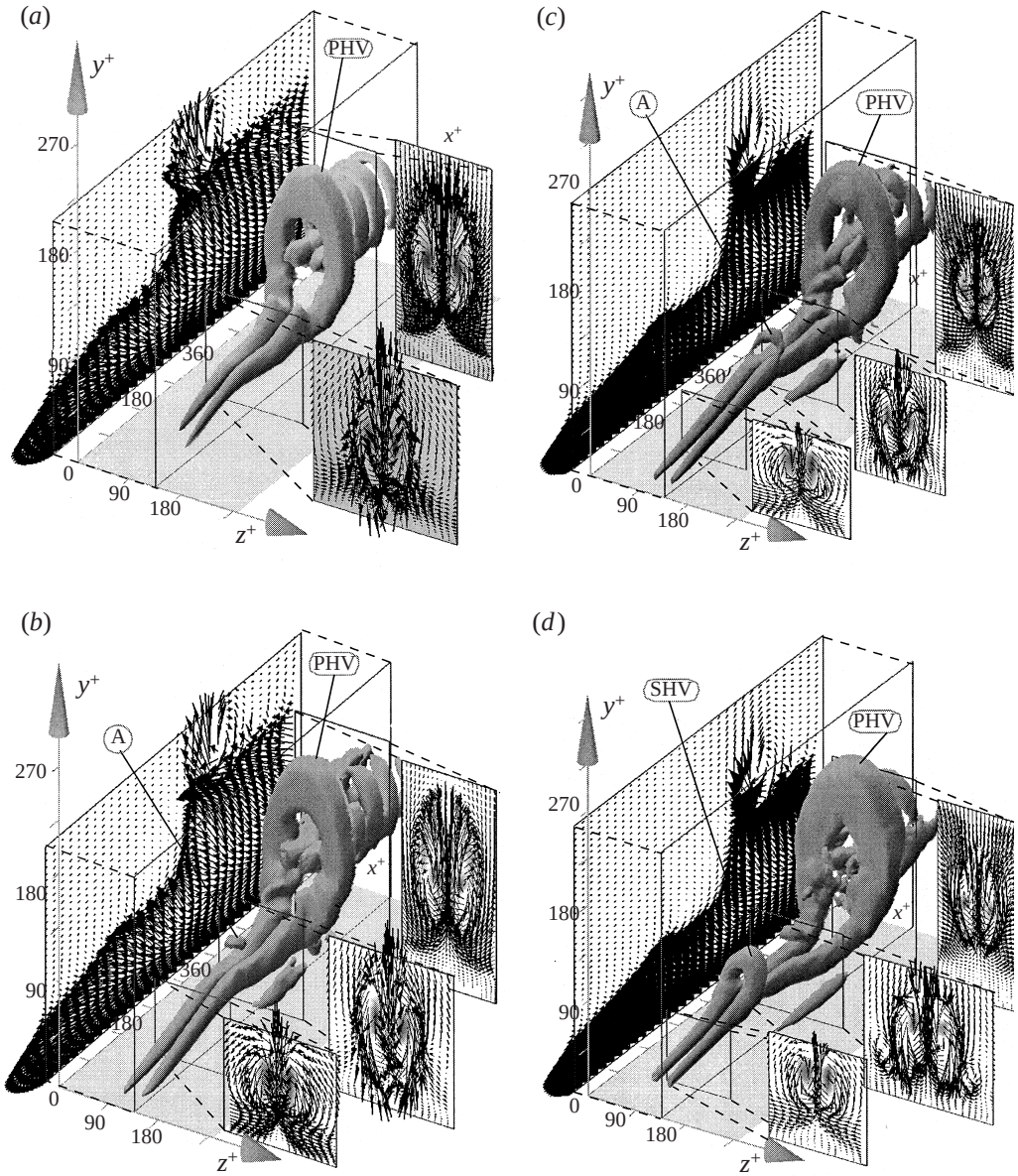

FIGURE 9. The generation of a secondary hairpin vortex follows the formation of the Ω-shaped head of the primary hairpin vortex shown in figure 7(*c*). The hairpin structures are identified with iso-surfaces of λ_{ci}^2 set at 3% of maximum at (*a*) $t^+ = 63$; (*b*) $t^+ = 72$; (*c*) $t^+ = 81$; (*d*) $t^+ = 117$. PHV, primary hairpin vortex, SHV, secondary hairpin vortex; SVA, spanwise vortex arch. Also plotted are vector plots of perturbation velocity on selected (x, y) and (y, z)-planes. Again, only a section of the entire computational domain surrounding the vortex structures is shown.

middle segments. This kink can be seen clearly at the points labelled *E* in the vortical structure shown in figure 8(*c*).

The kink is very similar in nature to the rapid change in slope observed during the formation of the primary hairpin vortex at the point where the near-horizontal downstream vortical tongues attach to the newly forming primary hairpin vortex.

The upstream segment plays the role of tilted Λ-shaped quasi-streamwise legs and the middle segment resembles the downstream vortical tongues. Thus, the subsequent evolution of the quasi-streamwise vortex pair near the kink follows along the same process as the one described in § 3.1 concerning the formation of the primary hairpin. It results in the generation of a secondary hairpin structure. The strong Q2 pumping of the near-wall fluid encounters the high-speed free-stream fluid to form an intense shear layer. This shear layer is located slightly above the vortex legs, and it is concentrated along the (x, y)-midplane passing between the vortex legs. The shear layer is particularly strong near the kink, since at the kink the vortex legs are at their closest approach. This part of the shear layer quickly rolls up into a compact spanwise vortex structure just above the kink, which can be clearly seen in figures 9(*b*) and 9(*c*) (marked A), corresponding to $t^+ = 72$ and 81. The spanwise vortex aids in the further lift-up of the streamwise vortex pair near the kink and in the sharpening of the kink. Quickly, as can be seen in figure 9(*d*) at $t^+ = 117$, the two long streamwise vortex legs break-off near the kink, and the upstream pair viscously connects with the rolled-up spanwise vortex to form the secondary hairpin vortex (SHV), which is detached from the legs of the primary hairpin vortex.

At this stage, the secondary hairpin vortex very much resembles the primary hairpin vortex at its initial stage of formation. The upstream sections of the vortex legs are about 140 viscous wall units long and have a shallow positive inclination of about 8°, while the downstream sections, which are about 50 viscous wall units long, have a steeper inclination of about 40°. Along the spanwise direction, the centres of the streamwise vortex pair are separated by about 40 viscous wall units near the downstream end and by about 100 viscous wall units near the upstream end, thus giving the vortex pair a characteristic *Λ*-shape. The only significant difference between the formation of the primary and secondary hairpins is that the upstream end of the secondary vortex legs is at a higher elevation of $y^+ = 45$, but its height still remains comparable at 50 viscous wall units.

The primary hairpin vortex is fully grown and its head has reached the channel centreline at $y^+ = 180$ by $t^+ = 117$. The head of the primary vortex has the characteristic near-vertical tilt of about 75°. The upstream end of the primary hairpin vortex legs, as a result of the vortex break-up process, has a small negative tilt of about −5°. These legs are about 190 viscous wall units in length and are at an elevation of about $y^+ = 45$. The overall streamwise extent of the primary hairpin vortex is about 330 viscous wall units, which is also approximately the streamwise separation between the primary and secondary vortex heads. The corresponding vertical separation between the two vortex heads is about 90 viscous wall units. Thus, the line joining the head of the primary and secondary vortices, which roughly characterizes the envelope of the vortical packet formed by the primary and secondary vortices, has a characteristic slope of 15° (see the schematic in figure 14*d*).

This process can be followed still further in time and figure 10 shows the vortex structure at a much later time of $t^+ = 297$. Figures 10(*a*), 10(*b*) and 10(*c*) show this complex vortex structure in three-dimensional perspective, side view, and top view, respectively. At this time, the secondary vortex is also fully grown and it has given way to the formation of a tertiary vortex. The formation of the tertiary vortex from the legs of the secondary hairpin vortex follows along the same lines as the formation of the secondary vortex from the legs of the primary hairpin vortex. It can be seen that the heads of the three hairpin vortices are located at $y^+ = 90$, 170 and 245. Their streamwise separations are approximately the same at 450 viscous wall units. Thus, the upstream envelope of the composite vortical packet makes an angle of 10°.

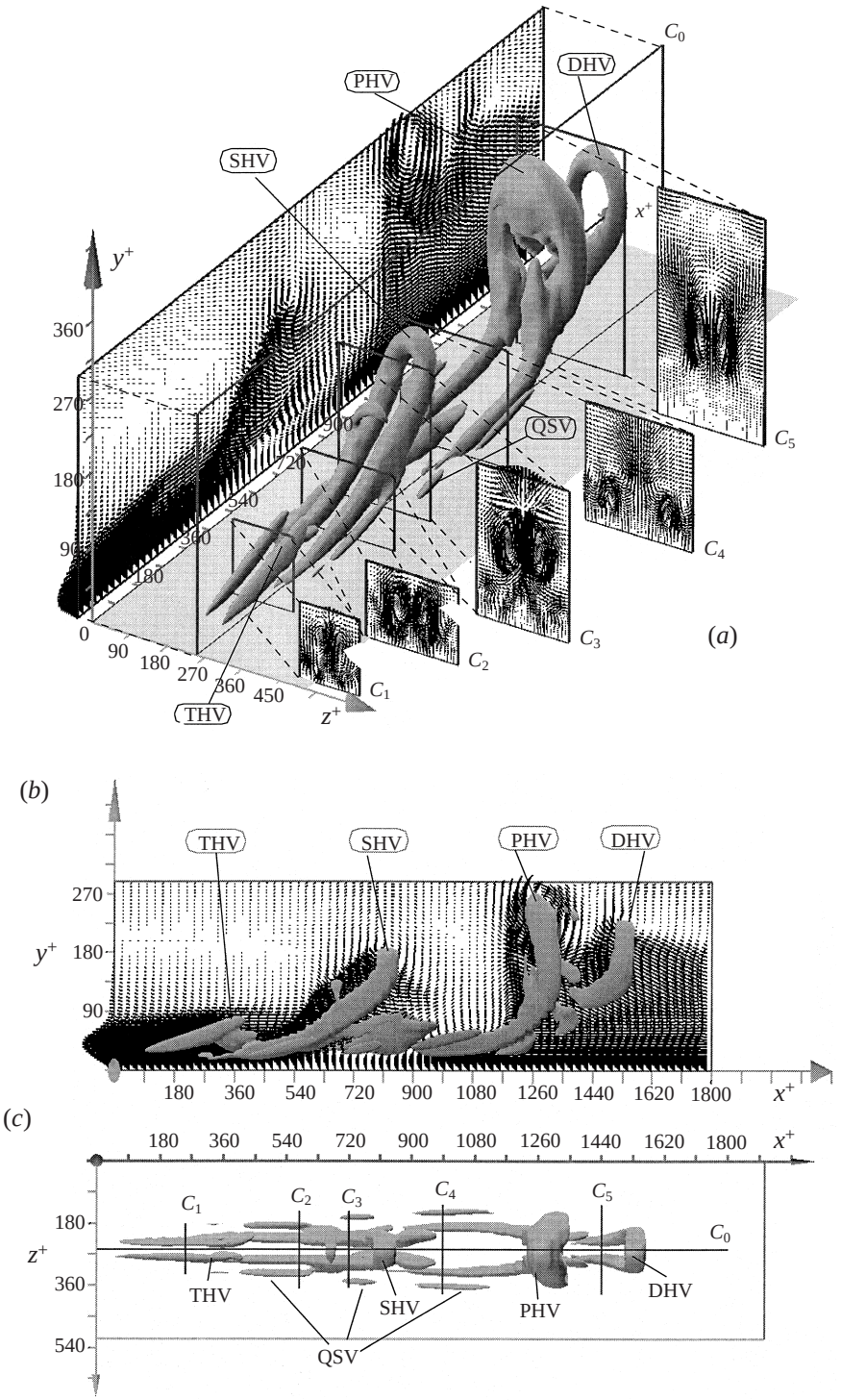

FIGURE 10. The sequence of vortices identified at $t^+ = 297$ by the iso-surface of λ_{ci}^2 with 2% of its maximum. (*a*) perspective view; (*b*) side view; (*c*) top view. The location of the five (z, y)-cross-sections (C_1–C_5) at $x^+ = 252$, 576, 720, 990, and 1440, shown in the perspective view (*a*) are also marked in the top view (*c*). The (x, y) velocity vector plots shown in (*a*) and (*b*) correspond to the spanwise centre of the box and cuts through the hairpin heads. PHV, primary hairpin vortex; SHV, sechondary hairpin vortex; THV, tertiary hairpin vortex; DHV, downstream hairpin vortex; QSV, quasi-streamwise vortices.

While the lengths of the primary and secondary vortices are slightly longer than 450 viscous wall units, at this stage the length of the tertiary hairpin vortex is only about 300 viscous units. It must be cautioned that at this time the head of the primary vortex is past the channel centreline so that its location and its vertical orientation are somewhat affected by the top of the channel. In the top view, the spanwise distance between the quasi-streamwise legs of the hairpin vortices can be seen to decrease from the primary to the secondary to the tertiary vortex. Also marked in this top view are vertical lines marking the location of the five (y, z)-planes on which the corresponding velocity vector plots are shown in figure 10(*a*).

3.5. *Formation and development of downstream hairpin vortices*

Apart from the primary, secondary and tertiary hairpin vortices, in figure 10, an additional hairpin vortex downstream of the primary hairpin vortex can be clearly observed. It is the result of the near-horizontal downstream vortical tongue seen during the early development of the primary hairpin vortex (see figures 4 and 5). This downstream hairpin vortex can be tracked back to as early as $t^+ = 45$. During the early period, the downstream vortical tongues develop rapidly into multiple downstream hairpin vortices. Two such downstream hairpin vortices can be seen in figures 7(*b*) and 7(*c*). A closer look at their formation process shows that the vortical tongues seen in figures 4(*b*) and 5(*c*) first stretch in the streamwise direction, and then tilt up to evolve into a hairpin vortex. This process of shear-layer roll-up and vortex connection is identical to the process that forms the primary hairpin vortex, but it happens on a much faster scale, owing to the close proximity and strong influence of the primary hairpin vortex. The strong Q4 velocity induced downstream of the primary hairpin vortex head interacts with the Q2 velocity induced by the downstream vortical tongues to create an intense shear layer. The shear layer rapidly rolls up and reconnects with the vortical tongues, resulting in the speedy formation of the downstream hairpin vortex. Once formed, the first downstream hairpin vortex rapidly evolves into a system of multiple downstream vortices. There is a brief window of time (see figures 9*a* and 9*b*) during which three downstream hairpin vortices are visible. The two downstream hairpins that are closer to the primary are relatively weak and they subsequently merge back with the primary hairpin, leaving only one downstream hairpin vortex visible in figure 10 at $t^+ = 297$.

During the early stages of formation, the legs of the downstream hairpin vortices are at an approximate elevation of about $y^+ = 80$. At around $t^+ = 108$, shown in figure 9(*d*), the length of the downstream hairpin vortex is about 100 viscous wall units, which is also nearly the downstream separation between the heads of the primary and downstream hairpin vortices. The head of the downstream hairpin vortex is located at $y^+ = 155$ and thus the downstream front of the envelope of the hairpin packet makes an angle of about -17°. At $t^+ = 297$, the legs of the downstream hairpin vortex have grown to 200 viscous wall units in length. The legs are also significantly lifted away from the wall and are at an approximate elevation of $y^+ = 100$. The head of the downstream vortex is approximately 220 viscous wall units downstream of the primary vortex head and is at an elevation of $y^+ = 215$. Thus, the composite vortical structure, while forming an angle of 10° upstream of the primary hairpin vortex, forms an approximate angle of about -7° downstream of the primary vortex.

3.6. *Growth rate and the threshold behaviour*

It must be pointed out that the above scenario of primary hairpin vortex formation and its subsequent evolution leading to the formation of secondary and tertiary hairpin

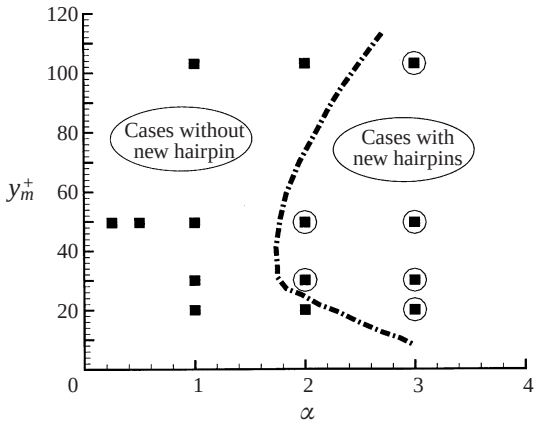

FIGURE 11. The generation of secondary hairpin vortices depends on the strength α and location y_m^+ of the event vector used to extract the initial vortical structures. A threshold behaviour in initial strength for the formation of secondary hairpin vortices can be identified.

vortices is for the case of an initial vortex of strength, $\alpha = 3.0$, located at $y_m^+ = 49.6$. Whereas the initial structure evolves into an Ω-shaped primary vortex, irrespective of its initial strength, α, and initial location, y_m^+, the autogeneration of secondary and tertiary vortices is quite sensitive to the amplitude. The autoregeneration process is possible only in the case of strong initial structures. Figure 11 shows in the (α, y_m^+) space the various cases considered and those for which the vortex regeneration process was observed. From this figure a threshold behaviour in the initial strength, α, for the vortex regeneration process is evident. It also appears from this figure that the threshold amplitude reaches a minimum for an initial location y_m^+ of around 30.

The presence of an optimum distance from the wall for the initial structure is not entirely surprising. This can be explained on the basis of the delicate balance between self- and mutual-induced motion of the quasi-streamwise vortex legs which tends to lift-up and curl back the vortices and the influence of mean shear which stretches along the streamwise direction and intensifies the vortices. Very close to the wall, viscous effects are also important. The enhanced viscous effects result in an increase in the threshold amplitude for initial vortices starting very close to the boundary. Whereas, away from the wall, the induced motion is determined by the strength of the vortex structure and streamwise stretching by the mean shear. With increasing distance from the wall, the mean shear rapidly reduces, thereby decreasing the intensification of the initial vortex structure by stretching. Thus, an initial hairpin vortex farther away from the boundary needs to be of sufficiently higher strength to generate subsequent hairpin vortices. The significant role played by the mean shear suggests that the details of the hairpin regeneration process can be different in laminar and turbulent boundary layers. For example, the threshold amplitude for regeneration, frequency of regeneration and the size and shape of the resulting hairpins can be influenced by the laminar or turbulent nature of the boundary layer and parameters such as Reynolds number and streamwise pressure gradient. In this regard, it should be noted that the background mean flow in the experiments by Haidari & Smith (1994) was a laminar Blasius profile.

Haidari & Smith (1994) observed that with very weak impulsive injection no hairpin vortex was formed. At moderate levels of injection, a hairpin vortex was formed, which subsequently was observed to evolve downstream and generate new

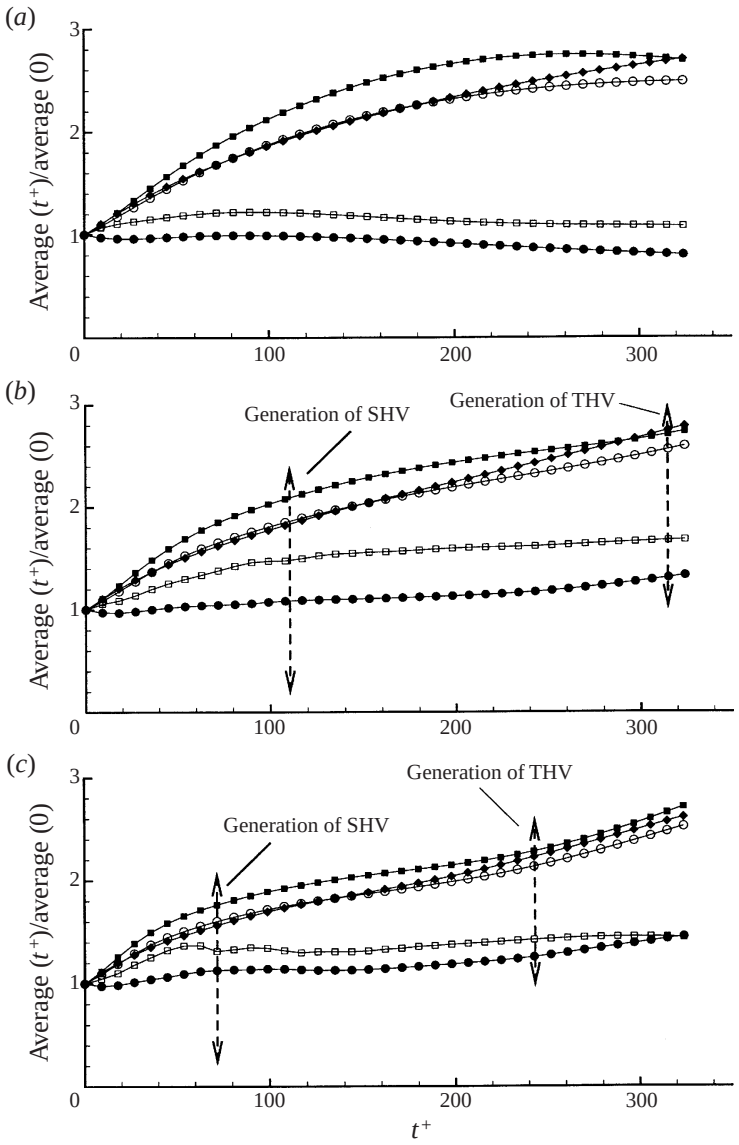

FIGURE 12. Growth rate of volume-averaged values: □, $|-u'v'|$; ●, $|\omega_x|$; ◆, $|\omega_y|$; ■, $|\omega_z'|$, and the magnitude of perturbation vorticity ○, $|\omega'|$ normalized by their initial values, for the initial structure shown in figure 4(*a*). (*a*) $\alpha = 1.0$; (*b*) $\alpha = 2.0$; (*c*) $\alpha = 3.0$. $y_m^+ = 49.6$.

hairpin vortices. Above a threshold, multiple hairpins were formed just as a result of the injection process. In contrast, here the simulations always started with a single hairpin-like vortical structure, whose initial strength was varied. Below a threshold amplitude, no additional vortices were generated, but, above the threshold amplitude, new hairpin vortices were observed to form. Thus, the threshold behaviour observed here is of a different nature from the threshold behaviour considered by Haidari & Smith (1994).

Evolution of the initial structure is followed in figures 12, where the volume averaged magnitude of Reynolds shear stress, $|-u'v'|$, streamwise and wall normal

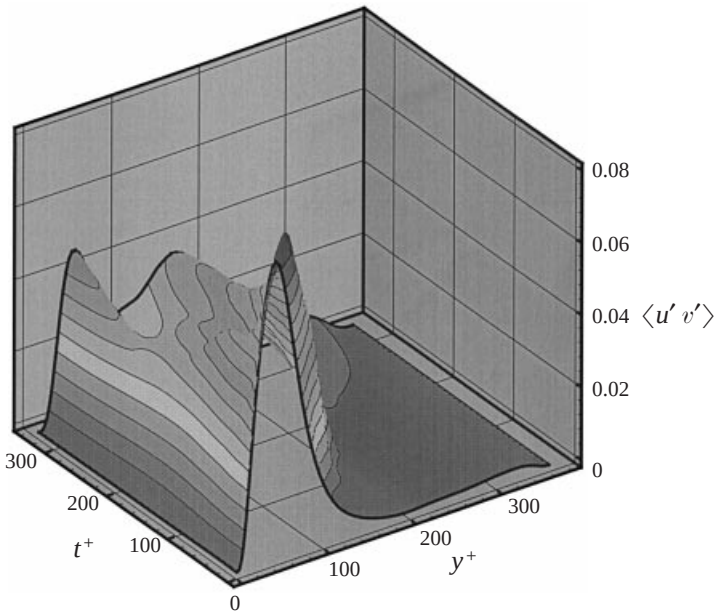

FIGURE 13. The variation with time and distance from the wall of the disturbation of (x, y)-averaged Reynolds shear stress, $\overline{u'v'}$. The initial structure for this plot is that shown in figure 4(*a*).

vorticity, $|\omega_x|$ and $|\omega_y|$, mean subtracted spanwise vorticity perturbation, $|\omega_z'|$, and perturbation vorticity magnitude, $|\omega'| = (\omega_x^2 + \omega_y^2 + \omega_z'^2)^{1/2}$, are plotted against time. Three different cases of initial location $y_m^+ = 29$ and amplitude, $\alpha = 1.0$, 2.0, and 3.0, respectively, are considered in figures 12(*a*), 12(*b*) and 12(*c*). Each quantity is normalized by its initial volume average. In the low-amplitude case, $\alpha = 1.0$, the normalized Reynolds stress reaches a weak maximum at around $t^+ \approx 80$ which corresponds approximately to the formation of the primary hairpin vortex structure. The perturbation vorticity magnitude evolves on a longer timescale, and appears to saturate around $t^+ \approx 300$. The vertical component of vorticity continues to increase over time, which during the initial period was supported by the formation and growth of the primary hairpin vortex. During the later stage ($t^+ \geqslant 225$), when the primary hairpin vortex has saturated, as shown by the perturbation vorticity magnitude, the growth in the vertical component of vorticity is balanced by a corresponding decrease in the streamwise component. This suggests a progressive tilting of the primary vortex to a near-vertical orientation without much intensification. Subsequently, the low-amplitude cases that are below the threshold exhibit a long and slow decay of the primary vortex structure. No secondary and tertiary vortices are observed in these cases. Nevertheless, even in these cases, the primary vortex, although weakening over time, remains coherent for a long time.

For initial amplitudes higher than the threshold (figures 12(*b*) and 12(*c*)), the evolution of the vortex structure in the beginning stages remains qualitatively the same as the lower-amplitude case, resulting in the formation of the primary Ω-shaped vortex. At sufficiently longer time, owing to the vortex regeneration process, the perturbation vorticity magnitude continues to increase. A corresponding increase in both the streamwise and wall normal components of vorticity can be observed. The plot of the Reynolds shear stress also illustrates the ability of the stronger initial vortical structure to increase and maintain a higher level of Reynolds stress through

the self-sustained autogeneration process. Also indicated in the figure are approximate times for the generation of secondary and tertiary hairpin vortices. Figure 13 shows a carpet plot of instantaneous Reynolds shear stress averaged over horizontal planes plotted as a function of t^+ and y^+. At the initial time, a single peak corresponding to the quasi-streamwise vortices can be seen around $y^+ = 50$. As the structure lifts and forms the primary hairpin vortex, the elevation of the peak Reynolds stress also increases. After $t^+ = 100$, the distribution associated with the primary vortex evolves more slowly, suggesting that the vortex has reached an equilibrium shape after a rapid transient from the initial condition. At later times, the peak corresponding to the primary can still be identified, although it has decreased in magnitude to about 0.04 and broadened a bit. A second peak in the Reynolds stress distribution can be seen for $t^+ \geqslant 200$, and this is associated with the secondary hairpin vortex. The Reynolds stress contribution from the concentrated secondary hairpin vortex quickly surpasses that of the somewhat diffused primary hairpin vortex.

3.7. *Comparison with experimental results*

A diagram illustrating the development of the initial vortex structure leading to the formation of secondary, tertiary and downstream vortices is shown in figure 14, where the five frames correspond approximately to times, $t^+ \cong 0$, 25, 50, 120, and 300, respectively. The different vortical structures marked, PH, SH, TH, DH, and VT correspond to primary hairpin, secondary hairpin, tertiary hairpin, downstream hairpin, and vortical tongue. Characteristic dimensions of the different hairpin structures are marked in these schematics. A tendency towards self-similar development of the hairpins can be observed. In particular, the shape and structure of the secondary hairpin during its early development at $t^+ \cong 120$ approximately resembles the initial state of the primary hairpin vortex. Their streamwise length is approximately 200 wall units and the upstream and downstream ends of the hairpin are respectively tilted at 8° and 25° to the horizontal. Vertical location is somewhat different in the two cases, possibly owing to the arbitrary location of the initial structure. This observation provides additional support to indicate that the stochastically estimated initial structures used in the present study are successful in extracting the generic behaviour of hairpin vortices.

At $t^+ \cong 120$ the primary hairpin is approximately 330 wall units downstream of the secondary, which is also the approximate length of the primary hairpin. This is somewhat larger than the experimental measurement of 100–150 wall units for the average streamwise distance between successive hairpin heads (Acarlar & Smith 1987; Meinhart *et al.* 1999). In figure 14, the angle that a line connecting the head of the primary and secondary vortices makes with the horizontal is about 15°. This compares well with the experimental observation of about 20° between vortex heads by Brown & Thomas (1977) and Head & Bandyopadhyay (1981) in a turbulent boundary layer and with an angle of 15° to 30° seen by Acarlar & Smith (1987*b*) in a laminar boundary layer. Based on a convective velocity for the hairpin of about 80% of free-stream velocity, Bandyopadhyay (1980) provided an estimate of 18.4° for this angle. It must be cautioned that the hot-wire measurements of Brown & Thomas (1977) and smoke visualization of Head & Bandyopadhyay (1981) extracted the inclination of large outer scale structures that defines the interface between the turbulent and non-turbulent regions of the boundary layer. The present result suggests that this angle could remain the same in the near-wall region as well.

At a later time, corresponding to $t^+ \cong 300$, a sequence of self-similar hairpin vortices can be seen, and they are separated by approximately 450 wall units along the

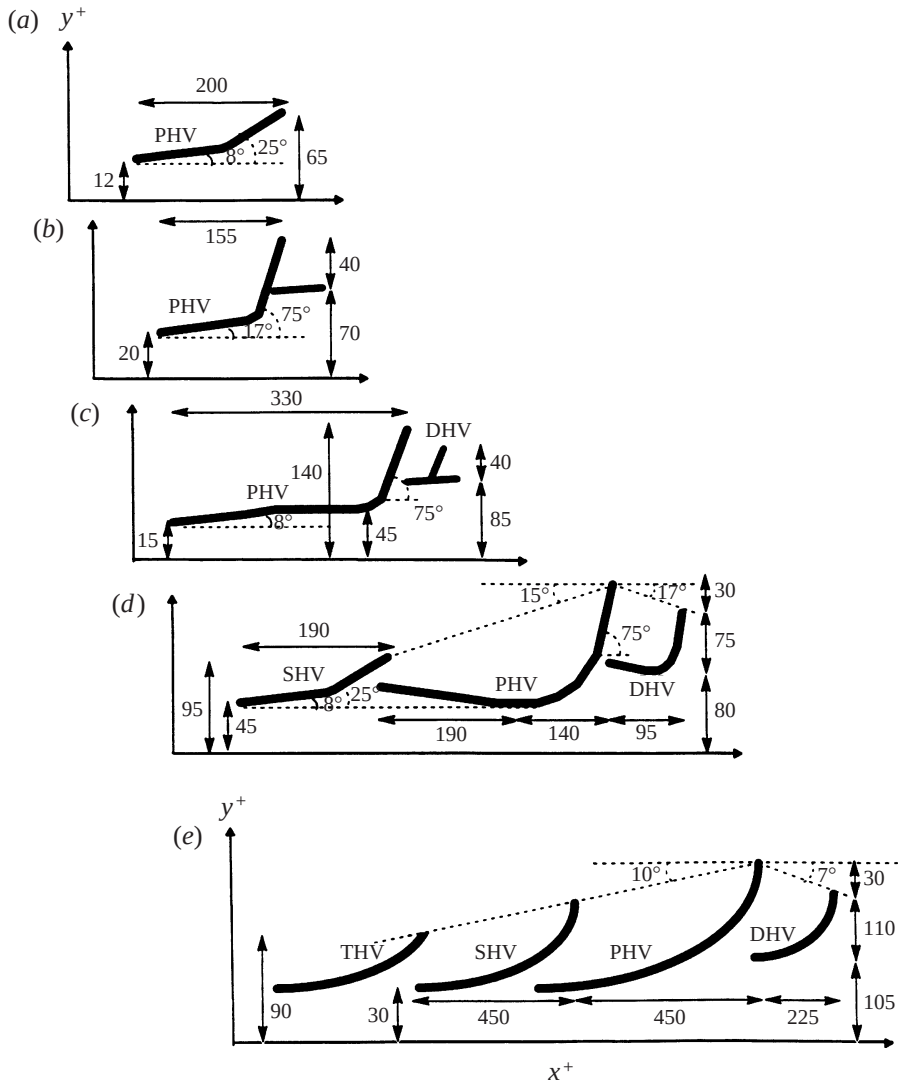

FIGURE 14. The growth and development of the hairpin vortex pocket at (*a*) $t^+ \approx 0$; (*b*) $t^+ \approx 25$; (*c*) $t^+ \approx 50$; (*d*) $t^+ \approx 120$; (*e*) $t^+ \approx 300$. Shown in this figure are the characteristic dimensions of the different hairpin structures.

streamwise direction. This is still larger than the experimentally observed streamwise separation between hairpin heads within a packet. It will be seen in § 3.10 that the streamwise distance between successive hairpins within a packet significantly decreases and compares favourably with experimental results as the asymmetry of the hairpins about the spanwise midplane increases. This suggests that the increased streamwise distance between the hairpins observed in the present computations is the result of assumed spanwise symmetry.

The computed angle of 10° for the upstream envelope of the packet seems lower. This quantitative discrepancy at later times is primarily due to the low-Reynolds-number turbulent channel flow considered here versus the high-Reynolds-number turbulent boundary layer considered by Bandyopadhyay (1980), Brown & Thomas

(1977) and Head & Bandyopadhyay (1981). In the present computations, the head of the primary hairpins rapidly rises and approaches the channel centreline. Owing to negligible mean shear near the centreline, the hairpin head takes a near-vertical orientation. In fact, at later times the hairpin head slightly crosses the centreline and further lift-up is inhibited. This behaviour provides a reasonable explanation for the shallow angle and large separation between hairpins observed at later times in the computation.

Further comparisons can be made with earlier experimental observations. In the side view, each individual hairpin is tilted up and the tilt angle varies from about 8° in the long quasi-streamwise legs to about 75° at the downstream end of the hairpin head. In comparison, Haidari & Smith (1994) report the angle to vary from about 6° at the upstream portion of the vortex legs to about 67° near the vortex head. A characteristic tilt of 45° is often quoted for hairpin heads (cf. Head & Bandyopadhyay 1981). From figure 14(*d*), it can be seen that with an approximate streamwise length and wall normal height of 140 wall units, the average tilt of the primary hairpin head is consistent with 45°.

The plan view of the vortex structure (figure 10*c*) shows that the average spanwise distance between the quasi-streamwise vortex legs is about 100 viscous wall units. The spanwise separation for the primary hairpin legs is somewhat greater than 100 wall units, but the separation decreases in the case of secondary, tertiary and downstream hairpin vortices. This increase in spanwise separation of the legs with the age of the hairpin is associated with the lift-up of the vortex legs. Close to the boundary, the effect of the image vortices is to bring the vortex legs together and decrease their spanwise separation. In many experiments, over a wide range of Reynolds numbers, the mean spanwise spacing between low-speed steaks in the sublayer region has been observed to be approximately 100 wall units (cf. Robinson 1991).

A velocity vector plot on a streamwise vertical (or x, y) plane located between the quasi-streamwise legs and cutting through the heads of the hairpins at $t^+ = 297$ is shown in figure 15(*a*). A constant velocity of 80% of the centreline velocity has been subtracted in this plot in order to correspond approximately to the frame of reference moving with the hairpin heads. The heads of the primary, secondary, tertiary, and downstream hairpins, marked by circles, are located approximately 240, 175, 90, and 215 wall units away from the bottom boundary, respectively. A corresponding velocity vector plot on a streamwise-wall normal plane obtained from high resolution PIV measurement in a zero-pressure-gradient turbulent boundary layer at $Re_\theta = 930$ (Meinhart *et al.* 1999) is shown in figure 15(*b*). Here again, a constant velocity of 80% of the free-stream velocity has been subtracted and the vortex heads are circled and marked A, B, C and D. As pointed out earlier, the streamwise separation between the hairpins is different between the computations and experiments; nevertheless, the coherency of the hairpins and their organization into a hairpin packet is clear in both cases. Even though, in the experimental measurement, it is hard to pinpoint which are the primary, secondary, and downstream hairpins, the general tendency to form additional vortices both upstream and downstream of a strong hairpin can be seen.

In both cases, a strong near-horizontal backflow that extends from the wall to about $y^+ > 30$ can be seen. The low-speed streak extends along the streamwise direction over distances much longer than an individual hairpin. Such observations of very long low-speed streaks very near the wall have previously been made by many researchers (for example Kreplin & Ecklemann 1979; Morrison & Kronauer 1969). Our results show that streaks can extend much higher. At low Re_θ the streaks are low, but at higher Re_θ streaks as large as $1200y^+$ have been observed. From the present

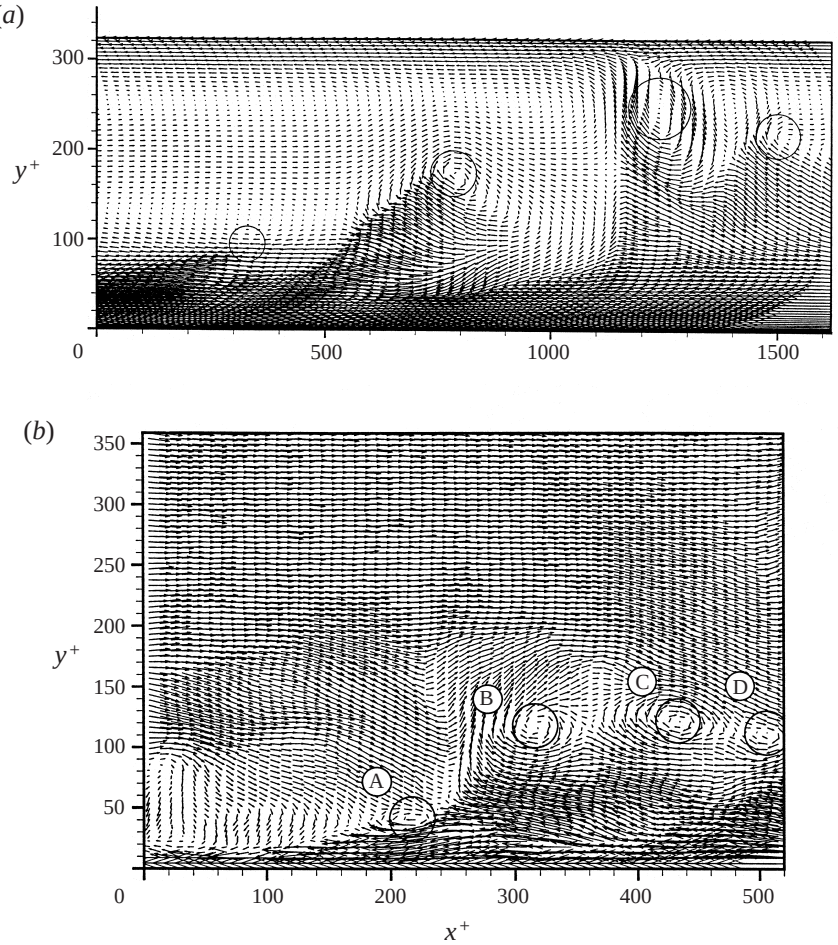

FIGURE 15. (*a*) Vector plot of velocity on the (x, y) symmetry plane at $t^+ = 288$. A constant streamwise velocity of 80% of centreline velocity has been subtracted. (*b*) Velocity vector plot on a streamwise–wall normal plane obtained from a high-resolutin PIV measurement of a zero-pressure-gradient boundary layer with $Re_\theta = 930$. A constant velocity of $U_c = 0.8\ U_\infty$ is subtracted form the streamwise velocity in order to bring out the packet of hairpins marked A, B, C, and D more clearly (see Zhou *et al.* 1997).

results it is clear that the cooperative backward pumping of the near-wall fluid by the streamwise aligned hairpins within a packet is one possible mechanism for the creation of near-wall streaks. It has previously been argued that the long near-wall low-speed streaks are the footprint of streamwise motion (or dragging) of relatively shorter quasi-streamwise vortices. Unlike this mechanism, the proposed explanation based on the collective action of a packet of hairpins requires no lasting memory of the near-wall fluid after the quasi-streamwise vortex has passed by.

3.8. *Generation of quasi-streamwise vortices*

In figures 3 and 9, a new pair of quasi-streamwise vortices straddling the legs of the primary hairpin vortex can also be seen. After the primary hairpin vortex legs lift, and before the secondary hairpin vortex forms, significant spanwise motion of the legs of the primary hairpin vortex is observed. Figure 16 is an end-view of velocity

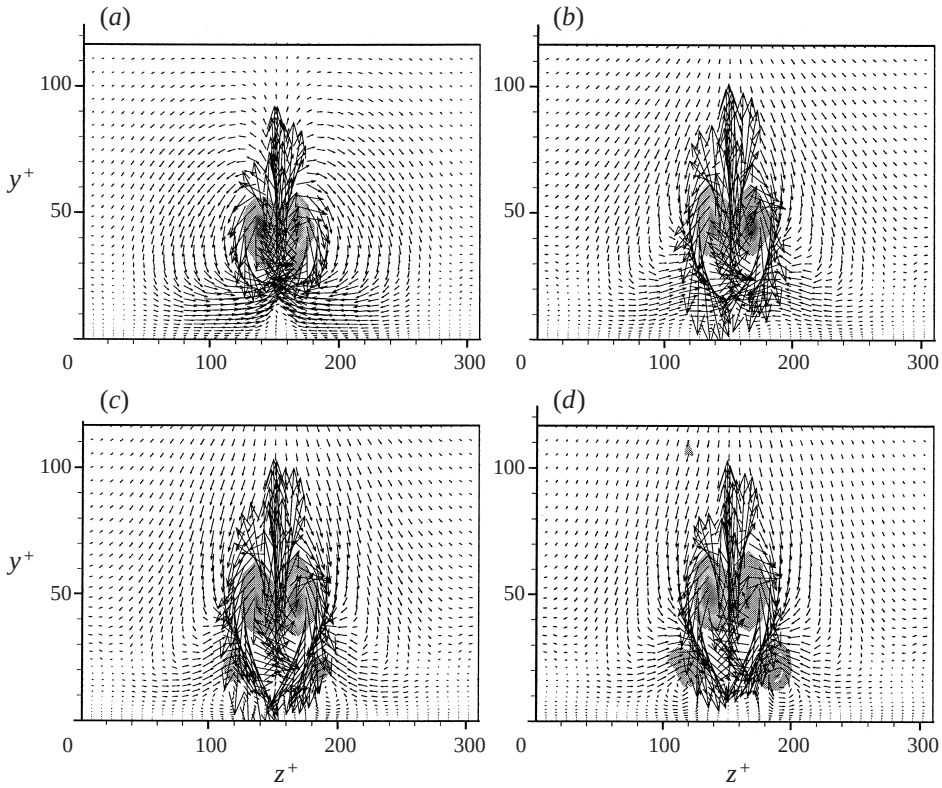

FIGURE 16. The generation of new quasi-streamwise vortices. The grey-level contours indicate the strength of the local streamwise vorticity, ω_x. Also plotted are the (w, v) velocity vectors on the (z, y)-plane located near the kinks or secondary hairpin vortex (see figure 9) at (*a*) $t^+ = 54$; (*b*) $t^+ = 63$; (*c*) $t^+ = 72$; (*d*) $t^+ = 81$.

field at $t^+ = 54$ around the location where the two legs of the primary hairpin vortex move towards each other. Also plotted in the figure are the shaded contours of the streamwise component of vorticity. The spanwise motion of the hairpin vortex legs along with the enhanced downward flow on their outboard side associated with the lift-up process, forms a pair of vorticity layers of concentrated streamwise vorticity. Near the wall, the vorticity layers arise from the no-slip condition at the bottom boundary of the channel. Their streamwise vorticity is opposite to that of the corresponding primary vortex leg. The effect of the wall can be represented by an image vorticity field, which drives the vorticity layers away from each other. On the other hand, the induced motion due to primary vortex legs pulls the two vorticity patches towards each other. As a result, the vorticity layers remain at approximately the same location until the legs of the primary vortex start to lift up. From figure 9, it can be seen that this lift-up process is associated with the formation of the secondary hairpin. The corresponding end view at $t^+ = 63$ is shown in figure 16 (*b*). It can be seen in this figure that the vorticity patches are in the beginning stages of roll-up into compact vortices. This roll up process can be followed over time, shown in figures 16(*c*) and 16(*d*) corresponding to $t^+ = 72$ and 81, resulting in the formation of fully mature newly formed streamwise vortices.

The creation of new quasi-streamwise vortices adjacent to existing streamwise vortex structures has been observed previously by Acarlar & Smith (1987*b*), Brooke

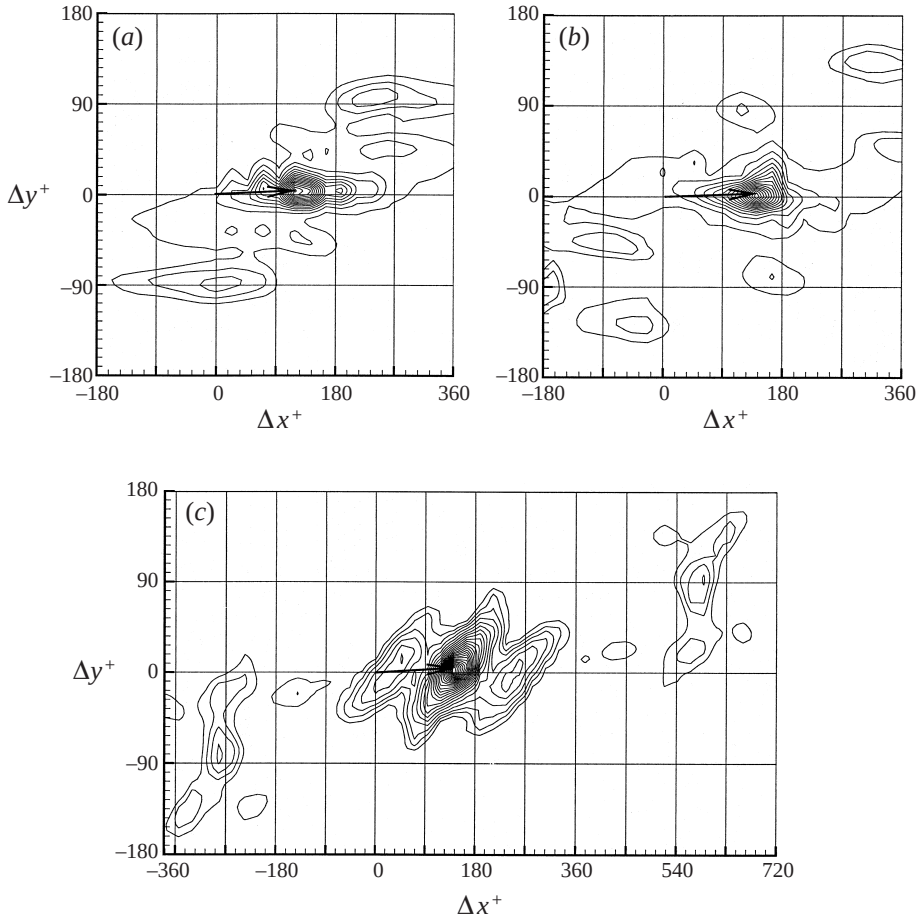

FIGURE 17. Space–time correlation function of swirling strength, $R_{\lambda\lambda}(\Delta x^+, \Delta y^+, \Delta t^+ = 9)$ at (*a*) $t^+ = 63$; (*b*) $t^+ = 117$; (*c*) $t^+ = 180$.

& Hanratty (1993), Bernard *et al.* (1993) and Jimenez & Orlandi (1993). Acarlar & Smith (1987*b*) suggested that the secondary streamwise vortices form beyond the saddle point on the wall kinematically generated by the primary streamwise vortex. This does not seem to be the case in the present simulations during the initial stages of formation of the new streamwise vortex. However, after the complete formation of the secondary streamwise vortex, a saddle point can be clearly seen between the old and new streamwise vortices (see figure 16*d*).

3.9. *Convective velocity of the hairpin vortices*

The convective velocity of the hairpin structures plays an important role in their proper characterization. In particular, since the vortex packet is made up of different hairpins that are at different stages in their evolution they may advect at different velocity. This in turn determines whether the packet remains coherent for a long time or disperses quickly. Furthermore, since in the computations the individual vortices and the hairpin packet as a whole are constantly in the process of development, any change in their advection velocity over time must also be accounted for.

To evaluate the convection velocity we compute the two-point correlation function

with a short time delay. Two-point space–time correlation of the vortex swirling strength is defined as

$$R_{\lambda\lambda}(r_x^+, r_y^+, t^+, \Delta t^+) = \iiint \lambda_{ci}(\boldsymbol{x}^+, t^+)\lambda_{ci}(\boldsymbol{x}^+ + \boldsymbol{r}^+, t^+ + \Delta t^+)\mathrm{d}\boldsymbol{x}^+, \tag{12}$$

where $\boldsymbol{r}^+ = (r_x^+, r_y^+, 0)$ is the spatial separation between the two points in viscous wall units, here restricted to be on the (x, y)-plane and the temporal separation, Δt^+, is set to be equal to 9. This choice of temporal separation was chosen so that it is large enough to measure accurately the velocity of the convecting vortical structures but small enough to capture the variation in the convection velocity with time. Figure 17(*a*) shows a contour plot of the two-point short-time-delayed correlation at $t^+ = 63$, plotted against the streamwise and wall normal separation. Three different peaks can be observed: a large central one, flanked on either side by a smaller peak. The multiple peaks in the correlation are due to the presence of a downstream hairpin in addition to the primary hairpin. The secondary and tertiary vortices have not formed at this instant in time. The central peak corresponds to the correlation of the primary hairpin at $t^+ = 63$ with itself after the small time separation of 9 viscous units. The correlation of the downstream hairpin with itself also contributed to this central peak. The cross-correlation of the primary and downstream hairpins at the first instance with the downstream and primary hairpins of the later time instance contributed, respectively, to the two smaller peaks which are on either side of the primary.

The location of the central peak at $r_x = 118$ and $r_y = 6$ corresponds to a streamwise velocity of 13 viscous units, which is nearly 72% of the centreline velocity of 18 in viscous units. The presence of a single coherent peak, in spite of the superposition of the self correlation of both the primary and downstream hairpin vortices, suggests that these two hairpin structures are advecting at about the same convection velocity. A non-zero vertical displacement for the peak correlation reflects the lift-up of the hairpin structures, but the rate of lift-up is significantly smaller than streamwise advection. The secondary peaks are a factor 10 smaller than the central peak and the locations of the secondary peaks, as one would expect, are symmetric about the central peak at $r_x = 1$, $r_y = -90$ and $r_z = 235$, $r_v = 97$. Based on the location of these smaller peaks, the horizontal and vertical separation between the primary and downstream vortex heads can be estimated as approximately 120 and 90 viscous wall units, respectively.

The contour plot of the two-point, short-time-delayed correlation at $t^+ = 117$, after the generation of the secondary hairpin, is shown in figure 17(*b*). By this time, the secondary vortex has formed. Again, a strong focused central peak can be observed, indicating that there is no significant dispersion between the different hairpin vortices. From the location of the peak, the streamwise velocity of the hairpin structures can be estimated to be 15.7, which is about 87% of the mean turbulent channel centreline velocity. Apart from the central peak, other local peaks of smaller magnitude can also be seen and they are associated with the cross-correlation between the primary, secondary, and downstream hairpins. The contour plot of the two-point short-time-delayed correlation at $t^+ = 288$, after the generation of the tertiary hairpin, is shown in figure 17. Convection velocity of the packet is nearly the same as before at 15.7 in viscous wall units.

The focused central peak in all the contour plots suggests that the different hairpins within the packet travel downstream at nearly the same convection velocity. On the other hand, figures 14(*d*) and 14(*e*) show that the streamwise separation between the primary and secondary hairpin heads has increased from about 330 to 450 viscous wall

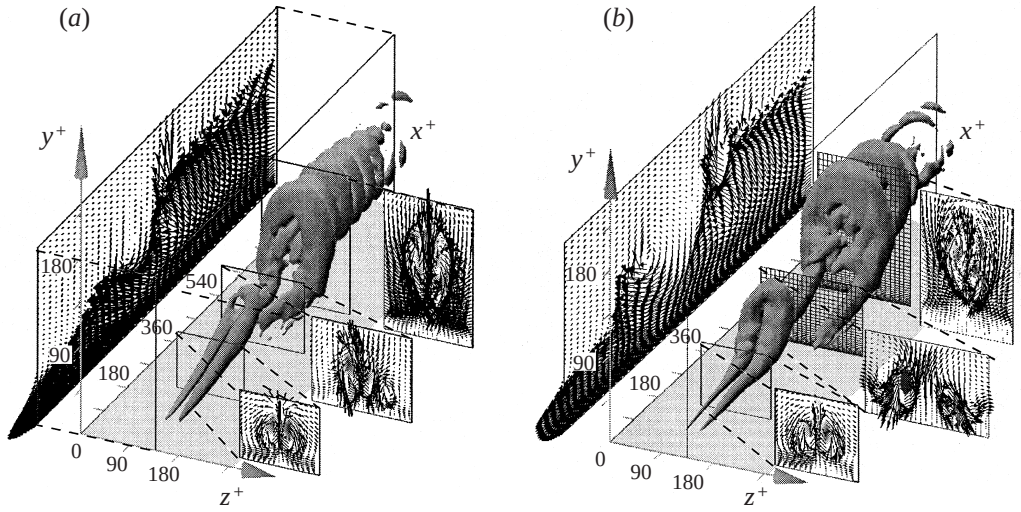

FIGURE 18. Generation of asymmetric secondary and downstream hairpin vortices from an initial structure extracted by an asymmetric event vector of $\alpha = 2$ specified at $y_m^+ = 30$, with a small spanwise component given by an asymmetry parameter of $\beta = 0.0625$. (*a*) $t^+ = 72$; (*b*) $t^+ = 108$.

units as the packet evolves from $t^+ \cong 120$ to $t^+ \cong 300$. This corresponds to a small dispersive velocity of 0.66, in wall units, which is only 3.5% of the mean centreline velocity. In comparison to the dispersion, during this time the packet would have travelled a distance of about 3000 viscous wall units along the streamwise direction. It thus appears that while a slow dispersion may not be ruled out, by and large the hairpin packet remains coherent during its evolution.

3.10. *Asymmetric hairpin structures*

In the present simulations the perfect streamwise alignment of the hairpins is the result of the spanwise symmetric nature of the initial vortex structure. In general, perfect symmetry cannot be expected, and as a result the hairpin vortices will not perfectly align along the streamwise direction. The effect of asymmetry on the evolution of the initial vortical structure and its development into a hairpin packet has been investigated. Asymmetry was introduced in the initial vortical structure with an asymmetric event in the stochastic estimation procedure. The magnitude of the event vector was kept constant in order to maintain the strength of the initial vortex structure approximately the same, while the spanwise component of the event vector was increased from zero at the expense of the u- and v-components. In particular, a series of simulations was performed with the event vector, $u_i = [7.78(1-\beta^2)^{1/2}, 1.76(1-\beta^2)^{1/2}, 8.0\beta]$, specified at $y_m^+ = 30.3$, for varying β, where β is the asymmetry parameter which measures the strength of asymmetry. For $\beta = 0$ there is no asymmetry and the initial vortex structure is the same as that shown in figure 6(*a*), but as the asymmetry parameter increases, the strength of the event vector is still the same.

The influence of asymmetry on the overall evolution of the hairpin structures remains negligibly small for an asymmetry parameter smaller than 0.125. Shown in figure 18 are the perspective views of the hairpin packet at $t^+ = 72$ and 108 for an asymmetry parameter of $\beta = 0.0625$. The initial structure has developed into a primary hairpin followed by the generation of secondary and downstream hairpins. The resulting hairpin packet is nearly symmetric and it closely resembles

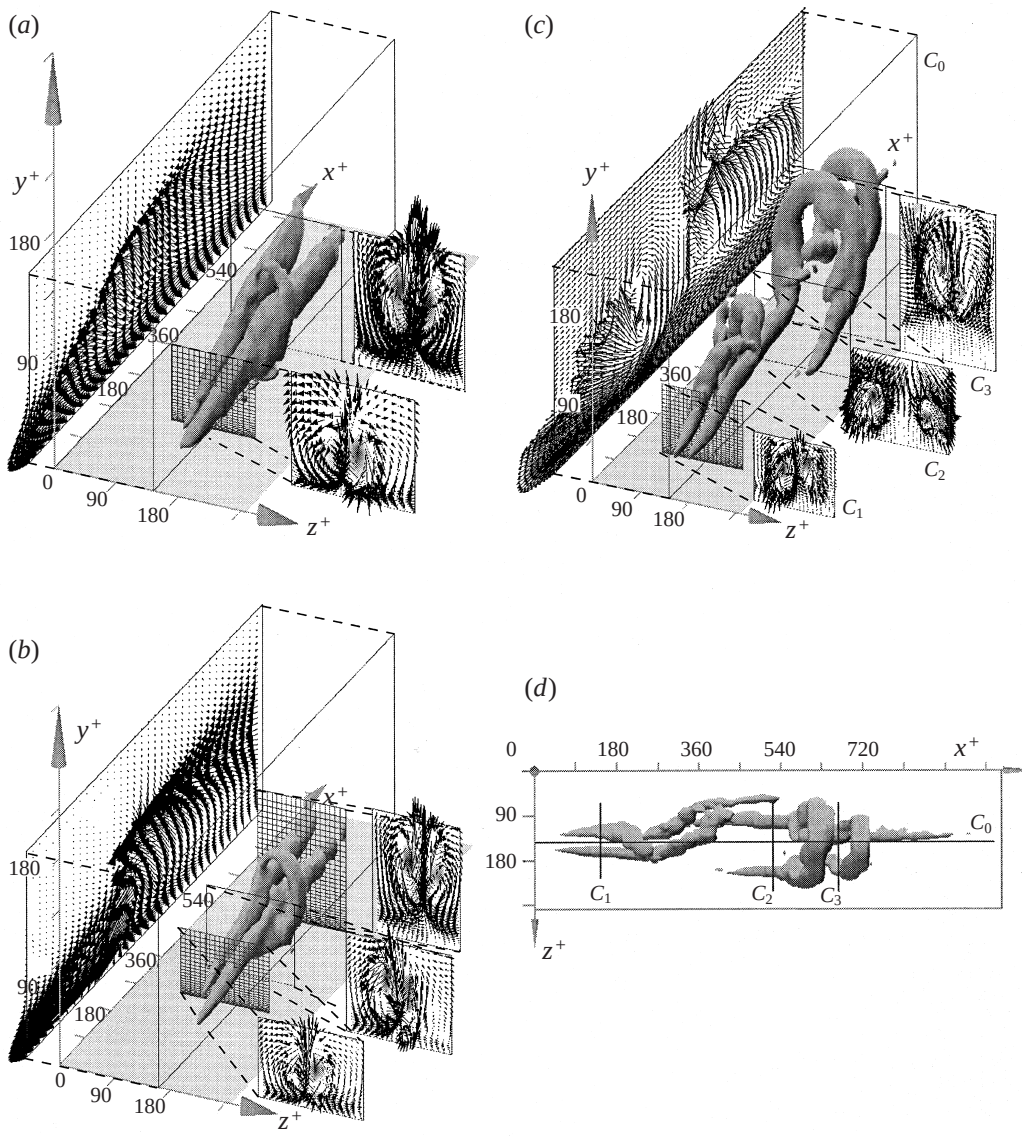

FIGURE 19. Generation of new asymmetric primary, secondary, tertiary, and downstream hairpin vortices from an initial asymmetric vortex structure extracted by an event vector of $\alpha = 2$ with asymmetry parameter $\beta = 0.25$ specified at $y_m^+ = 30$. (*a*) $t^+ = 27$; (*b*) $t^+ = 36$; (*c*) $t^+ = 144$; (*d*) the top view at $t^+ = 144$.

the hairpin packet generated under symmetric initial conditions (the evolution closely follows the sequence shown in figures 6(*a*)–6(*c*). Thus, the mechanisms responsible for autogeneration of new hairpin vortices leading to the formation of a hairpin packet remain largely unaffected by small asymmetry in the initial development.

With sufficiently strong asymmetry in the initial event vector, its effect can be distinguished in the initial structure as well as in the evolution. Vortical structure corresponding to an asymmetry parameter of $\beta = 0.25$ will be followed. The resulting initial structure has a pair of quasi-streamwise legs connected by a weak spanwise

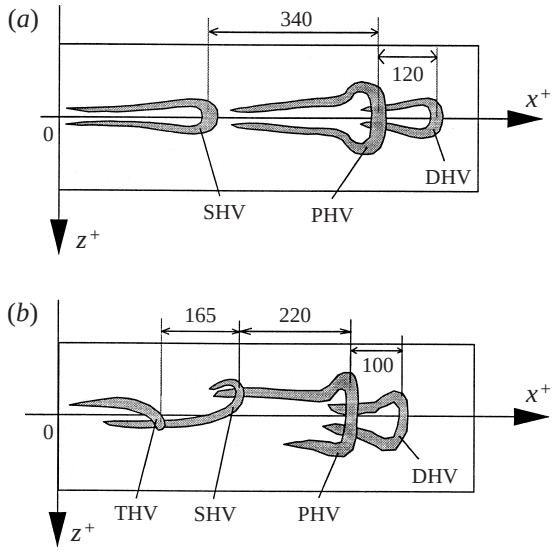

FIGURE 20. Top view of the hairpin packet at $t^+ = 144$ for an initial event vector of $\alpha = 2$ specified at $y_m^+ = 30$. (*a*) Symmetric case; (*b*) asymmetric case with asymmetry parameter $\beta = 0.25$.

bridge at the downstream end, but one of the quasi-streamwise legs is much stronger, higher, and longer than the other. A perspective view of the asymmetric structure at $t^+ = 27$ is shown in figure 19(*a*). The right-hand quasi-streamwise vortex leg is stronger than the left-hand one. The asymmetry persists as the initial structure evolves in time. A perspective view of the resulting structure at $t^+ = 36$ is shown in figure 19(*b*), where the initial vortex structure has developed into an asymmetric Ω-shaped structure. Otherwise, the initial development of the asymmetric Ω-shaped hairpin followed along the same lines as the symmetric initial condition. A pair of asymmetric downstream vortical tongues can also be seen.

Figure 19(*c*) shows the vortex structure at a much later time of $t^+ = 144$. At this instant, in addition to the primary hairpin, secondary and tertiary hairpin-like structures can also be seen. The right-hand leg of the secondary hairpin can be seen, while the other quasi-streamwise vortex leg is so weak that it is not seen. On the other hand, in the case of the tertiary hairpin only the left-hand quasi-streamwise leg is strong and visible. Therefore, the secondary and tertiary hairpins, resemble the asymmetric one-sided cane- or hook-like hairpin vortices often referred to in literature (Robinson 1991). These cane-like secondary and tertiary structures are clearly visible in the top view shown in figure 20(*b*). Based on experimental evidence Nishino, Kasagi & Hirata (1988) and Guezennec & Choi (1989) observe that quasi-streamwise vortices in the near-wall region occur most often singly and only rarely as counter-rotating pairs of equal strength. Through detailed probing of the DNS boundary-layer database (Spalart 1988), Robinson (1991) has pointed out that the preferred arrangement for hairpin vortices in a turbulent boundary layer is to be asymmetric and one-sided. The present results suggest that experimentally observed asymmetry is possibly due to the influence of local spanwise velocity.

The top view of the hairpin structure at $t^+ = 144$ for the corresponding symmetric case with initial event vector of $\alpha = 2$ specified at $y^+ = 30.3$ is shown in figure 20(*a*). As pointed out earlier, the streamwise distance of 340 viscous units between the primary and secondary hairpins in the symmetric case is significantly larger than

the experimentally measured separation of about 150 viscous wall units (Meinhart *et al.* 1999). Whereas, in the asymmetric case the streamwise distance between the primary and secondary and between the secondary and tertiary hairpin heads is about 220 and 165 viscous wall units, respectively. These streamwise separations compare better with the experimental measurements. Furthermore, in the asymmetric case the formation of tertiary hairpin is nearly complete by $t^+ = 144$. Whereas, in the symmetric case the tertiary hairpin has not even begun to form by this time. In general, it is observed that asymmetry aids in the formation of subsidiary hairpins. In fact, the initial threshold amplitude for the formation of secondary and tertiary hairpins appears to be somewhat lower with asymmetry. Under asymmetry, the new hairpins form more readily in rapid succession and their streamwise separation is smaller, in better comparison with the experiments.

4. Summary and conclusions

Viscous evolution of a single hairpin having strength and core diameter that are representative of vortex motion that occurs in near-wall boundary-layer turbulence has been studied in a background mean turbulent flow. The initial structure was obtained using a linear stochastic estimation procedure applied to the two-point correlation of a $Re_\tau = 180$ channel-flow direct-numerical-simulation database (Kim *et al.* 1987). The basic event vector employed in the stochastic estimation of the initial structure is a symmetric Q2 vector whose streamwise and wall normal velocity perturbations are determined based on maximum contribution to Reynolds shear stress. The magnitude of the event vector and its location were varied and correspondingly a wide range of strength and location of the initial structure was considered.

The stochastically estimated initial vortical structure consists of a counter-rotating pair of symmetric quasi-streamwise vortices that are tilted up with their upstream end close to the wall and their downstream end away from the wall. The quasi-streamwise vortices are connected at their downstream end by a narrow spanwise bridge whose strength increases as the location of the initial event vector moves away from the boundary. This initial vortical structure always develops into a classical hairpin-shaped vortex with an Ω-shaped head and a pair of counter-rotating long quasi-streamwise vortex legs that are connected to the head by a neck region. The strength and location of the initial event vector only determine the speed at which this formation process proceeds; stronger initial structure develops into the fully formed hairpin vortex more rapidly.

The subsequent development of the primary hairpin vortex exhibits a threshold behaviour. Primary vortices of strength below this threshold are observed to maintain their structural integrity for hundreds of viscous timescales but undergo a very slow decay process, without the generation of any additional structures. Stronger initial vortices, on the other hand, result in the generation of a secondary hairpin vortex on its upstream side. The mechanism behind the generation of the secondary hairpin very much resembles the formation of the primary hairpin. A kink forms in the long legs of the primary hairpin vortex owing to the mutual induction process. The shear layer that forms between the long legs is at its peak strength near the kink. While the shear layer rolls-up into a compact spanwise vortex, the long legs of the primary vortex sever near the kink. The upstream sections of the legs viscously connect with the rolled-up spanwise vortex to form the secondary hairpin vortex. The secondary hairpin, in turn, results in the generation of a tertiary hairpin upstream of it. The process by which these additional vortices are generated also proceeds along similar lines to

those observed for primary and secondary vortices. The threshold behaviour is a clear indication of the importance of nonlinearity in the formation of hairpin vortices.

The computational results indicate the existence of an optimal wall normal location for the initial vortical structure where the threshold amplitude for the generation of new hairpin vortices is at its minimum. This can be explained on the basis of the delicate balance between self-induced and mutually induced motion of the quasi-streamwise vortex legs which tend to lift the vortices up and back, and the influence of mean shear which stretches and intensifies the vortices along the streamwise direction. In general, it can be expected that if the hairpin is initially strong it will quickly lead to the generation of a new hairpin. If the initial hairpin is weak, it needs to lift-up more and gain sufficient strength before it can generate a new hairpin. Below the threshold initial strength, the hairpin does not lift up enough to gain sufficient strength to generate a new hairpin. Based on these observations, the following hypothesis can now be made about the generation process of hairpin vortices in a turbulent boundary layer. *Only a sufficiently strong hairpin vortex results in the formation of a new hairpin.* Weaker ones decay without offspring. The age at which a hairpin gives birth to a new one depends on its initial strength. Stronger hairpins generate newer ones sooner than weaker hairpins.

The probability that hairpin vortices strong enough to generate subsequent hairpin vortices occur in a natural turbulent boundary layer needs to be considered. The strength of the initial vortex structure relative to the typical local turbulent fluctuation is dependent on the magnitude of the event vector. For example, the symmetric Q2 event vector for amplitude $\alpha = 1$ corresponds to a peak Reynolds shear stress of $u_m v_m \approx -2\sigma_u\sigma_v$, where σ_u and σ_v are the r.m.s. streamwise and wall normal velocity components based on the data of Moin *et al.* (1987). This estimate is only weakly dependent on the y-location of the event vector. This suggests that for $\alpha = 1$ the peak Reynolds shear stress is about five times the mean Reynolds shear stress, $\overline{uv}$ (here we have used the standard turbulent wall-layer estimate that $\overline{uv} \approx 0.4\,\sigma_u\sigma_v$). The peak Reynolds shear stress for the stronger initial structures with $\alpha = 2$ and $\alpha = 3$ correspondingly scale up to 20 and 45 times $\overline{uv}$, respectively. Although the average Reynolds shear stress increases as the initial hairpin structure evolves (see figure 12), in general, the peak value decreases with time. The increase in the average Reynolds shear stress is due to the growth in size of the hairpin packet. The peak Reynolds shear stress increases in magnitude only during the formation of secondary and tertiary hairpin structures, but never becomes larger than its initial value.

There is ample experimental evidence to indicate that such large Reynolds stress excursions from the mean are common and typical of bursts associated with a packet of hairpin vortices. The dominant contribution to the mean Reynolds shear stress is during periods of rapid outward bursts from the near-wall region. Their frequency of occurrence is such that the conditional average of the Reynolds shear stress during the burst process can be an order magnitude larger than $\overline{uv}$. Blackwelder & Kaplan (1976) measured the conditional average to be about 10 $\overline{uv}$. The instantaneous peak Reynolds shear stress within the burst process can, in fact, be even higher. For instance, Nychas, Hershey & Brodkey (1973) have reported instantaneous values of $\overline{uv}$ as high as 40 $\overline{uv}$. Even higher instantaneous Reynolds shear stress of the order $uv \approx 62\ \overline{uv}$ have been reported by Willmarth & Lu (1972). It is therefore reasonable to consider that event vectors with $\alpha = 2$ and $\alpha = 3$ provide initial structures whose magnitude are consistent with experimentally observed hairpin packets.

The formation of new hairpins on the upstream side of a mature hairpin vortex has previously been addressed by Smith and coworkers (Haidari & Smith 1994;

Smith *et al.* 1991). The present observations of the regeneration process are in general agreement with their pioneering work. The direct numerical solutions of the Navier–Stokes equations have allowed us to follow closely the vortex break-up and viscous reconnection processes. In addition to the secondary and tertiary vortices, new hairpins also form on the downstream side of the primary hairpin vortex. The generation of new hairpin vortices on the downstream side appears to have never been previously reported. Here, we observe that the downstream vortices grow out of a pair of quasi-streamwise vortical tongues that stick out from the head of the primary hairpin on the downstream side. While this at first might look surprising and appear as an artifact of the stochastically estimated initial condition, there is strong evidence that these downstream vortical tongues are realistic features of a typical hairpin. The flow visualizations of Haidari & Smith (1994) show clear evidence of quasi-streamwise vortical tongues to the downstream side of their initial hairpin structures. The first downstream hairpin vortex, once formed, has a pair of downstream vortical tongues of its own, which rapidly evolve into a second downstream hairpin vortex. This process continues, resulting in the generation of several downstream hairpin vortices in quick succession, but most of these hairpins are relatively weak and undergo rapid decay.

The primary hairpin and the newly formed hairpins have a definite spatial relationship and together they form a coherent hairpin packet. The envelope of the composite vortical structure has a tent-like appearance forming an angle of 10° to 15° upstream of the primary hairpin and an angle of about −7° to −15° downstream of the primary hairpin. The instantaneous velocity vector plot corresponding to the hairpin packet on an (x, y)- plane passing through the centre of the hairpin heads is in excellent agreement with the experimental PIV measurements of Meinhart & Adrian (1995) and Meinhart *et al.* (1999). These instantaneous planar ((x, y)-plane) experimental velocity measurements taken over a range of Reynolds numbers confirm the existence of coherent packet of hairpin vortices in a turbulent wall layer. Moreover, the experimental data reveal signatures corresponding to hairpin packets in over 70% of the realizations. Thus, packets appear to be a very common occurrence in natural boundary layers. This is not to say that they are the only mechanism, but that they do occur frequently.

Three factors in the present work make it possible to observe hairpin packets: the use of contours of λ_{ci}^2 to visualize the eddies, the growth of the packets in a clean background flow unobscured by other eddies and/or interactions with other eddies, and the use of Gallilean reference frames. Even so, once one recognizes the hairpin packet paradigm, it becomes possible to observe the packets in fully turbulent data sets. For example, Robinsons's (1991, 1993) figures when reexamined show signatures of hairpins occurring in succession, although they are surrounded by a clutter of other vortices and vortex fragments. Work in progress in our group has also shown that hairpin packets are readily found in DNS at $Re_\tau = 395$, although they are surrounded by many other eddies. The significance of hairpin packets in the total structure of wall turbulence must be established by future work.

Within the hairpin packet, the individual hairpins have a nearly self-similar structure. The individual hairpins are tilted up, with the tilt angle varying from about 8° at the upstream end of the quasi-streamwise vortex legs to about 75° at the downstream end of the hairpin head. The average tilt angle is about 45°, in agreement with the results of Head & Bandyopadhyay (1981), Acarlar & Smith (1987 *a*, *b*) and Haidari & Smith (1994).

A near-wall inclined shear layer associated with each hairpin plays an important role in the generation of new hairpin vortices. The multiple Q2 signature associated

with the computed hairpin packet is consistent with the experimental measurement of multiple Q2 events during a burst process (Bogard & Tiederman 1986; Luchik & Tiederman 1987; Tardu 1995). As a consequence of the sequence of hairpin vortices aligned one behind the other along the streamwise direction, a long low-speed region forms between the legs of the hairpins in the near-wall region. While the individual vortices are observed to be about 400 viscous wall units in length along the streamwise direction, owing to the cooperative action between all the streamwise aligned hairpins, the resulting low-speed streak is observed to be significantly longer. Thus, the often observed long low-speed streaks are consistent with the existence of a coherent packet of hairpin vortices. However, there have been other mechanisms proposed to explain the near-wall low-speed streaks (see for example Jeong *et al.* 1997; Hamilton, Kim & Waleffe 1995). Recently Schoppa & Hussain (1997) illustrated that an initial condition consisting of a staggered pattern of streamwise vortices also leads to near-wall structures that are consistent with other numerical and experimental observations. If one restricts attention to the quasi-streamwise vortices in the near-wall region $y^+ \leqslant 60$, the geometric patterns and the lengthscale of the near-wall structures that arise from the development of an asymmetric hairpin vortex (shown in figures 19 and 20) are in reasonable agreement with those observed by Jeong *et al.* (1997) and Schoppa & Hussain (1997).

The robustness of the mechanism for generating new hairpins and the streamwise alignment of the resulting hairpins indicates that the turbulent boundary layer may not be completely described by a random distribution of hairpins of different sizes and ages as in Perry & Chong (1982) and Perry *et al.* (1986). Spatial coherence may exist between the neighbouring hairpins. The arrangement of the hairpins into groups or packets with definite size and age distribution has a potentially large effect on the transport properties of the hairpins. In a fully turbulent boundary layer, as the various hairpin packets grow, it is likely that they run into each other and interact in a complex manner and may decrease the level of organization. Furthermore, the outer-layer perturbations and other vortical debris, which are present in a turbulent boundary layer at higher Reynolds numbers, may also impact the coherence of the near-wall packets. The present simulations say nothing about interactions between groups of hairpins or about the effect of outer-layer perturbations on the level of internal coherence or organization within the near-wall packets. The present computations pertain only to the early phases of hairpin packet formation and therefore the results should only be applied to the near-wall layer up to several hundred viscous wall units. However, experimental evidence (Tomkins 1997) suggests that even at higher Reynolds numbers, streamwise coherence persists between the neighbouring near-wall vortical structures, in spite of what appears to be random organization of some of the outer structures. Thus, we believe that the organization of near-wall hairpin vortices is important even in a high-Reynolds-number fully turbulent flow. Clearly, further investigation is required to fully ascertain the quantitative effect of the turbulent large scale outer structures on the organization of near-wall hairpin vortices. Existing hairpin models such as Perry & Chong (1982) and Perry *et al.* (1986) can then be further strengthened by incorporating the effect of hairpin organization into packets.

A mechanism for the generation of quasi-streamwise vortices has also been identified. This mechanism involves the spanwise motion of the primary vortex legs along with the enhanced downward flow associated with its lift-up process, which forms a pair of near wall layers of concentrated streamwise vorticity. As the lift-up process continues, these patches of streamwise vorticity roll-up into coherent streamwise vortices. The streamwise vortices tend to form on the outboard side of the primary

vortex legs. The creation of new quasi-streamwise vortices besides existing streamwise vortex structures has previously been observed by many (Acarlar & Smith 1987*b*; Bernard *et al.* 1993; Brooke & Hanratty 1993; Jimenez & Orlandi 1993). The present generation mechanism is consistent with those proposed by Brooke & Hanratty (1993) and Bernard *et al.* (1993) based on detailed analysis of their DNS databases. The generation of additional quasi-streamwise vortices helps explain the frequent observation that the streamwise vortices are more populous than transverse vortices (cf. Robinson 1991).

The present results clearly establish the causes and effects and provide a mechanistic picture of the autogeneration process leading to the natural formation of hairpin packets. Furthermore, the resulting structure provides a reasonably unified picture of the turbulent near-wall region, capable of explaining many of the previously observed flow features. While the present simulations are performed at a low Reynolds number, we think that the coherent vortex packets are a fundamental flow feature of the near-wall region, even at higher Reynolds numbers. The experimental results of Meinhart *et al.* (1999) indicate that hairpin vortex packets are a common feature in the low-Reynolds-number near-wall region of high-Reynolds-number flows. The mechanisms for creating packets of hairpins show no strong sensitivity to outer flow conditions. The experimental results of Meinhart & Adrian (1995) and Urushihara, Meinhart & Adrian (1993) also show that hairpin vortex packets occur from the wall layer out to the logarithmic layer of turbulent boundary-layer flow and turbulent pipe flow. Thus, we conjecture that the results reported here can be applied to higher Reynolds number as well, although it must be allowed that some additional effects may occur.

This research was supported by the Air Force Office of Scientific Research, the Office of Naval Research and the National Science Foundation. Computations presented here were performed on a Cray C90 at the Pittsburgh Supercomputer Center.

REFERENCES

Acarlar, M. S. & Smith, C. R. 1987*a* A study of hairpin vortices in a laminar boundary layer. Part 1. Hairpin vortices generated by a hemisphere proturberance. *J. Fluid Mech.* **175**, 1–41.

Acarlar, M. S. & Smith, C. R. 1987*b* A study of hairpin vortices in a laminar boundary layer. Part 2. Hairpin vortices generated by fluid injection. *J. Fluid Mech.* **175**, 43–83.

Adrian, R. J. 1996 Stochastic estimation of the structure of turbulent fields. In *Eddy Structure Identification* (ed. J. P. Bonnet), pp. 145–196. Springer.

Adrian, R. J., Moin, P. & Moser, R. D. 1987 Stochastic estimation of conditional eddies in turbulent channel flow. In *Proc. 1987 Summer Program of the Center for Turbulence Research*, pp. 7–19. NASA Ames/Stanford University.

Bakewell, P. & Lumley, J. L. 1967 Viscous sublayer and adjacent wall region in a turbulent pipe flows. *Phys. Fluids* **10**, 1880–1889.

Bandyopadhyay, P. 1980 Large structure with a characteristic upstream interface in turbulent boundary layers. *Phys. Fluids* **23**, 2326–2327.

Batchelor, G. K. 1967 *Introduction to Fluid Dynamics*, pp. 509–511. Cambridge University Press.

Bernard, P. S., Thomas, J. M. & Handler, R. A. 1993 Vortex dynamics and the production of Reynolds stress. *J. Fluid Mech.* **253**, 385–419.

Blackwelder, R. F. & Kaplan, R. E. 1976 On the wall structure of the turbulent boundary layer. *J. Fluid Mech.* **76**, 89–112.

Bogard, D. G. & Tiederman, W. G. 1986 Burst detection with single-point velocity measurements. *J. Fluid Mech.* **162**, 389–413.

Brooke, J. W. & Hanratty, T. J. 1993 Origin of turbulence-producing eddies in a channel flow. *Phys. Fluids* A **5**, 1011–1022.

Brown, G. L. & Thomas, A. S. W. 1977 Large structure in a turbulent boundary layer. *Phys. Fluids* **20**, S243.

Chong, M. S., Perry, A. E. & Cantwell, B. J. 1990 A general classification of three-dimensional flow fields. *Phys. Fluids* A **2**, 765–777.

Dallman, U., Hilgenstock, A., Riedelbanh, S., Schulte-Werning, B. & Vollmers, H. 1991 On the footprints of three-dimensional separated vortex flows around blunt bodies. *AGARD Conf. Proc*. 494.

Guezennec, Y. G. & Choi, W. C. 1989 Stochastic estimation of coherent structures in turbulent boundary layers. In *Proc. Zoran P. Zaric Memorial International Seminar on Near Wall Turbulence, May 1988* (ed. S. J. Kline & N. H. Afgan), pp. 420–436. Hemisphere.

Haidari, A. H. & Smith, C. R. 1994 The generation and regeneration of single hairpin vortices. *J. Fluid Mech.* **277**, 135–162.

Hamilton, J. M., Kim, J. & Waleffe, F. 1995 Regeneration mechanisms of near-wall turbulence structures. *J. Fluid Mech.* **287**, 317–348.

Head, M. R. & Bandyopadhyay, P. 1981 New aspects of turbulent boundary layer structure. *J. Fluid Mech.* **107**, 297–338.

Hon, T.-L. & Walker, J. D. A. 1991 Evolution of hairpin vortices in a shear flow. *Comput. Fluids* **20**, 343–358.

Hunt, J. C. R., Wray, A. A. & Moin, P. 1988 Eddies, streams, and convergence zones in turbulent flows. In *Proc. 1988 Summer Program of the Center for Turbulence Research*, pp. 193–207. NASA Ames/Stanford University.

Jeong, J. & Hussain, F. 1995 On the identification of a vortex. *J. Fluid Mech.* **285**, 69–94.

Jeong, J., Hussain, F., Schoppa, W. & Kim, J. 1997 Coherent structures near the wall in a turbulent channel flow. *J. Fluid Mech.* **332**, 185.

Jimenez, J. & Orlandi, P. 1993 The rollup of a vortex layer near a wall. *J. Fluid Mech.* **248**, 297–313.

Kempka. S. N. 1988 Evolution of vortices in a turbulent boundary layer. PhD thesis, University of Illinois, Urbana, Illinois.

Kendall. T. M. 1992 Evolution of conditional eddies in channel flow. MS thesis, University of Illinois, Urbana, Illinois.

Kim, J. 1983 On the structure of wall-bounded turbulent flows. *Phys. Fluids* **26**, 2088–2097.

Kim, J. 1987 Evolution of a vortical structure associated with the bursting event in a channel flow. In *Turbulent Shear Flows 5* (ed. F. Durst, B. E. Launder, J. L. Lumley, F. W. Schmidt & J. H. Whitelaw), pp. 221–233. Springer.

Kim, J., Moin, P. & Moser, R. D. 1987 Turbulent statistics in fully developed channel flow at low Reynolds number. *J. Fluid Mech.* **177**, 133–166.

Kreplin, H. P. & Ecklemann, H. 1979 Behaviour of the three fluctuating velocity components in the wall region of a turbulent channel flow. *Phys. Fluids* **22**, 1233–1239.

Luchik, T. S. & Tiederman, W. G. 1987 Timescale and structure of ejections and bursts in turbulent channel flows. *J. Fluid Mech.* **174**, 529–552.

Meinhart, C. D. 1994 Investigation of turbulent boundary-layer structure using particle-image velocimetry. PhD thesis, University of Illinois, Urbana, Illinois.

Meinhart, C. D. & Adrian, R. J. 1995 On the existence of uniform momentum zones in a turbulent boundary layer. *Phys. Fluids* **7**, 694–696.

Meinhart, C. D., Adrian, R. J. & Tomkins, C. D. 1999 Vortex organization in the outer region of a turbulent boundary layer. (In preparation.)

Moin, P., Adrian, R. J. & Kim, J. 1987 Stochastic estimation of organized structures in turbulent channel flow. In *Proc. 6th Turbulent Shear Flow Symp.* pp. 16.9.1–16.9.8. Toulouse.

Moin, P., Leonard, A. & Kim, J. 1986 Evolution of a curved vortex filament into a vortex ring. *Phys. Fluids* **29**, 955–963.

Morrison, W. R. B. & Kronauer, R. E. 1969 Structure similarity for fully developed turbulence in smooth tubes. *J. Fluid Mech.* **39**, 117–141.

Nishino, K., Kasagi, N. & Hirata, M. 1988 Study of streamwise vortical structures in a two-dimensional turbulent channel flow by digital image processing. In *Transport Phenomena in Turbulent Flows* (ed. M. Hirata & N. Kasagi), pp. 157–170. Hemisphere.

Nychas, S. G., Hershey, H. C. & Brodkey, R. S. 1973 A visual study of turbulent shear flow. *J. Fluid Mech.* **61**, 513–540.

Perry, A. E. & Chong, M. S. 1982 On the mechanism of wall turbulence. *J. Fluid Mech.* **119**, 173–217.

Perry, A. E., Henbest, S. & Chong, M. S. 1986 A theoretical and experimental study of wall turbulence. *J. Fluid Mech.* **165**, 163–199.

Robinson, S. K. 1991 Coherent motions in the turbulent boundary layer. *Ann. Rev. Fluid Mech.* **23**, 601–639.

Robinson, S. K. 1993 The kinematics of turbulent boundary layer structures. *NASA Tech. Mem.* 103859.

Robinson, S. K., Kline, S. J. & Spalart, P. R. 1988 Statistical analysis of near-wall structures in turbulent channel flow. In *Proc. Zoran P. Zaric Memorial International Seminar on Near Wall Turbulence, May 1988* (ed. S. J. Kline & N. H. Afgan), pp. 218–247. Hemisphere.

Schoppa, W. & Hussain, F. 1997 Genesis and dynamics of coherent structures in near-wall turbulence: a new look. In *Self Sustaining Mechanisms of Wall Turbulence* (ed. R. L. Panton), pp. 385–422. Computational Mechanics Publications, Southampton, UK.

Singer, B. A. & Joslin, R. D. 1994 Metamorphosis of a hairpin vortex into a young turbulent spot. *Phys. Fluids* **6**, 3724–3736.

Smith, C. R. 1984 A synthesized model of the near-wall behavior in turbulent boundary layers. In *Proc. Eighth Symp. on Turbulence* (ed. G. K. Patterson & J. K. Zakin). University of Missouri-Rolla. Dept. of Chem. Engng, Rolla, Missouri.

Smith, C. R., Walker, J. D. A., Haidari, A. H. & Sobrun, U. 1991 On the dynamics of near-wall turbulence. *Phil. Trans. R. Soc. Lond.* A **336**, 131–175.

Soria, J. & Cantwell, B. J. 1993 Identification and classification of topological structures in free shear flows. *Eddy Structure Identification in Free Turbulent Shear Flows* (ed. J. P. Bonnet & M. N. Glauser), pp. 379–390.

Spalart, P. R. 1988 Direct numerical simulation of a turbulent boundary layer up to $R_\theta = 1410$. *J. Fluid Mech.* **187**, 61–98.

Tardu, F. 1995 Characteristics of single and clusters of bursting events in the inner layer. Part 1: Vita events. *Exps Fluids* **19**, 112–124.

Theodorsen, T. 1952 Mechanism of turbulence. In *Proc. Second Midwestern Conf. of Fluid Mechanics*, pp. 1–19. Ohio State University, Columbus, Ohio.

Tomkins, C. D. 1997 A particle image velocimetry of coherent structures in a turbulent boundary layer. MS thesis, University of Illinois, Urbana, Illinois.

Urushihara, T., Meinhart, C. D. & Adrian, R. J. 1993 Investigation of the logarithmic layer in pipe flow using particle image velocimetry. In *Near Wall Turbulent Flows* (ed. R. M. C. So, C. G. Speziale & B. E. Launder), pp. 433–446. Elsevier.

Willmarth, W. W. & Lu, S. S. 1972 Structure of the Reynolds stress near the wall. *J. Fluid Mech.* **55**, 65–92.

Zhong, J., Huang, T. & Adrian, R. J. 1996 Extracting 3D vortices in turbulent fluid flow. *IEEE Trans. on Pattern Analysis and Machine Intelligence* **20**, 193–199.

Zhou, J., Adrian, R. J. & Balachandar, S. 1996 Autogeneration of near wall vortical structure in channel flow. *Phys. Fluids* **8**, 288–291.

Zhou, J., Meinhart, C. D., Adrian, R. J. & Balachandar, S. 1997 Formation of hairpin pockets in wall turbulence. In *Self Sustaining Mechanisms of Wall Turbulence* (ed. R. L. Panton), pp. 109–134, Computational Mechanics Publications, Southampton, UK.